2019

Structural Insight into Layer Gliding and Lattice Distortion in Layered Manganese Oxide Electrodes for Potassium-Ion Batteries

Qing Zhang
University of Wollongong, qz964@uowmail.edu.au

Christophe R. Didier
University of Wollongong, *Australia Nuclear Science and Technology Organisation*, cdidier@uow.edu.au

Wei Kong Pang
University of Wollongong, wkpang@uow.edu.au

Yajie Liu
University of Wollongong, yl327@uowmail.edu.au

Zhijie Wang
University of Wollongong, zw110@uowmail.edu.au

See next page for additional authors

Publication Details

Zhang, Q., Didier, C., Pang, W., Liu, Y., Wang, Z., Li, S., Peterson, V. K., Mao, J. & Guo, Z. (2019). Structural Insight into Layer Gliding and Lattice Distortion in Layered Manganese Oxide Electrodes for Potassium-Ion Batteries. Advanced Energy Materials, 9 (30), 1900568-1-1900568-9.

Structural Insight into Layer Gliding and Lattice Distortion in Layered Manganese Oxide Electrodes for Potassium-Ion Batteries

Abstract

Potassium-ion batteries (PIBs) are an emerging, affordable, and environmentally friendly alternative to lithium-ion batteries, with their further development driven by the need for suitably performing electrode materials capable of reversibly accommodating the relatively large K+. Layer-structured manganese oxides are attractive as electrodes for PIBs, but suffer from structural instability and sluggish kinetics of K+ insertion/extraction, leading to poor rate capability. Herein, cobalt is successfully introduced at the manganese site in the KxMnO2 layered oxide electrode material and it is shown that with only 5% Co, the reversible capacity increases by 30% at 22 mA g-1 and by 92% at 440 mA g-1. In operando synchrotron X-ray diffraction reveals that Co suppresses Jahn-Teller distortion, leading to more isotropic migration pathways for K+ in the interlayer, thus enhancing the ionic diffusion and consequently, rate capability. The detailed analysis reveals that additional phase transitions and larger volume change occur in the Co-doped material as a result of layer gliding, with these associated with faster capacity decay, despite the overall capacity remaining higher than the pristine material, even after 500 cycles. These results assert the importance of understanding the detailed structural evolution that underpins performance that will inform the strategic design of electrode materials for high-performance PIBs.

Disciplines

Engineering | Physical Sciences and Mathematics

Publication Details

Zhang, Q., Didier, C., Pang, W., Liu, Y., Wang, Z., Li, S., Peterson, V. K., Mao, J. & Guo, Z. (2019). Structural Insight into Layer Gliding and Lattice Distortion in Layered Manganese Oxide Electrodes for Potassium-Ion Batteries. Advanced Energy Materials, 9 (30), 1900568-1-1900568-9.

Authors

Qing Zhang, Christophe R. Didier, Wei Kong Pang, Yajie Liu, Zhijie Wang, Sean Li, Vanessa K. Peterson, Jianfeng Mao, and Zaiping Guo

WILEY-VCH

DOI: 10.1002/((please add manuscript number))
Article type: Communication

Structural insight into layer gliding and lattice distortion in layered manganese oxide electrodes for potassium ion batteries

Qing Zhang, Christophe Didier, Wei Kong Pang, Yajie Liu, Zhijie Wang, Sean Li, Vanessa K. Peterson, Jianfeng Mao and Zaiping Guo **

Qing Zhang, Dr. Christophe Didier, Dr. Wei Kong Pang, Dr. Yajie Liu, Zhijie Wang, Prof. Vanessa K. Peterson, Dr. Jianfeng Mao*, and Prof. Zaiping Guo*
Institute for Superconducting & Electronic Materials, University of Wollongong, Wollongong, NSW 2522, Australia.
E-mail: jmao@uow.edu.au, zguo@uow.edu.au
Dr. Christophe Didier and Prof. Vanessa K. Peterson
Australia Nuclear Science and Technology Organisation, Lucas Heights, NSW 2234, Australia.
Prof. Sean Li
School of Materials Science and Engineering, The University of New South Wales, Kensington, New South Wales 2052, Australia.
Prof. Zaiping Guo and Prof. Vanessa K. Peterson
School of Mechanical, Materials, Mechatronics & Biomedical Engineering, University of Wollongong, NSW 2500, Australia.
Prof. Zaiping Guo
College of Chemistry and Chemical Engineering, Hubei University

Keywords: Potassium Ion Batteries, Cobalt Doping, Rate capability, Cooperative Jahn-Teller Distortions

Abstract: Potassium-ion batteries (PIBs) are an emerging, affordable, and environmentally-friendly alternative to lithium-ion batteries, with their further development driven by the need for suitably-performing electrode materials capable of reversibly accommodating the relatively large K^+. Layer-structured manganese oxides are attractive as electrodes for PIBs, but suffer from structural instability and sluggish kinetics of K^+ insertion/extraction, leading to poor rate capability. Herein, we successfully introduce cobalt at the manganese site in the K_xMnO_2 layered oxide electrode material and show that with only 5% Co the reversible capacity increases by 30% at 22 mA g^{-1} and by 92% at 440 mA g^{-1}. *In operando* synchrotron X-ray diffraction revealed that Co suppresses Jahn-Teller distortion, leading to more isotropic

migration pathways for K^+ in the interlayer, thus enhancing the ionic diffusion and consequently, rate capability. Our detailed analysis reveals that additional phase transitions and larger volume change occurs in the Co-doped material as a result of layer gliding, with these associated with faster capacity decay, despite the overall capacity remaining higher than the pristine material, even after 500 cycles. These results assert the importance of understanding the detailed structural evolution that underpins performance that will inform the strategic design of electrode materials for high-performance PIBs.

The efficient use of electricity generated from renewable energy sources is important in addressing rising global energy demands and environmental issues. The demand for improved energy storage is driven by commercial and industrial applications such as in portable electronic devices as well as the booming electric vehicle industry and load balancing of power grids. Current growth rates in lithium-ion battery (LIB) manufacturing are not sustainable given our limited lithium resources. In this context, alternative battery systems with low cost are sought, with sodium- and potassium-ion batteries (SIBs and PIBs, respectively) regarded as suitable replacements due to the high natural abundance of sodium and potassium and their similar working mechanism to LIBs.[1] Of these, PIBs are more promising due to the closeness of the K^+/K redox potential (-2.9 V *vs*. H^+/H_2O) to that of Li^+/Li (-3.0 V *vs*. H^+/H_2O), as compared to Na^+/Na (-2.7 V *vs*. H^+/H_2O), and the consequential ease of reversible K^+ intercalation into the most common LIB negative electrode, graphite.[2-4]

The slow kinetics of the reversible insertion of K^+ in electrode materials as a result of its relatively large ionic radius of 1.38 Å is a major issue for the realization of high performance PIBs.[5-7] For PIB technology to be successful, scientists need to find stable electrode materials capable of reversibly hosting K^+ relatively quickly. Transition metal layered oxides

possess a two-dimensional structure that can accommodate large ions and are attracting interest as potential PIB electrode materials.[8-14] Among these, manganese layered oxides are particularly promising due to the high natural abundance and non-toxicity of manganese. A range of layered K_xMnO_2 structure types can be prepared[15, 16] including orthorhombic P2 and P"2 types, the hexagonal P3-type, and the monoclinic P'3-type, whose formation can be controlled by synthesis conditions.[15] Reasonable electrochemical performance was reported for electrodes produced using $K_{0.3}MnO_2$ with the P2-type orthorhombic structure[17] and $K_{0.5}MnO_3$ with the P3-type hexagonal structure,[18] however, both these materials suffer from poor rate capability and have phase transformations at low K content that reduce cycle life. *In situ* X-ray powder diffraction of P3-type $K_{0.5}MnO_2$ showed the reversible transformation from the P3 to the O3-type structure at very low potassium content, with further K^+ extraction leading to irreversible transformation to an unknown structure.[18]

Strong cooperative Jahn-Teller distortions due to high-spin Mn^{3+} ($3d^4$) in layered Li_xMnO_2 and Na_xMnO_2 lead to lowering from rhombohedral to monoclinic symmetry and structural deterioration,[19, 20] with this likely to occur also in the layered K_xMnO_2 material. Transition metal doping has successfully addressed this issue in manganese layered oxides,[19-23] with the substitution of Mn^{3+} by Mg, Al, Ni, Cr, and Co reducing Jahn-Teller distortion in layered Li_xMnO_2 and Na_xMnO_2.[24, 25] However, the straightforward and successful approaches applied to LIBs/SIBs may not be suitable for PIBs because the larger K^+ induce more complex electrochemical behaviours and structural evolutions. Although several studies have examined transition metal substitution in K_xMnO_2, no detailed structural evolution upon electrochemical cycling was reported,[26-28] and the effects of Jahn-Teller distortion in layered K_xMnO_2 remain unknown. Therefore, further studies aimed to understand the K_xMnO_2 structure changes that occur upon charge/discharge cycling and further improve its electrochemical performance are highly desirable.

In this work, K_xMnO_2 with the monoclinic P'3-type structure was synthesized and evaluated as a PIB electrode. The reversible K^+ intercalation mechanism was investigated using *in operando* synchrotron X-ray powder diffraction (SXRPD) and the K^+ insertion mechanism found to differ to that of the related P3-type $K_{0.5}MnO_2$ material. Furthermore, the replacement of ~ 5% Mn with Co produced the P'3-type $K_xMn_{1-y}Co_yO_2$ electrode material, with enhanced rate cyclability and capacity retention within a PIB, as a result of reduced cooperative Jahn-Teller distortion. This work provides insights in the structural evolution of manganese-based layered electrode materials for PIBs, important to their development.

P'3-type pure and cobalt-doped K_xMnO_2 were synthesized by a sol-gel method. The structure of as-synthesized samples was examined using neutron powder diffraction (NPD) and X-ray powder diffraction (XRPD) as shown in Figure 1 and Figure S1, respectively. Data for K_xMnO_2 (Figure 1a, Figure S1a) could be indexed with a monoclinic unit-cell with lattice parameters a = 5.1313(4) Å, b = 2.84822(15) Å, c = 6.5976(4) Å, β = 103.898(5)° of space-group symmetry $C2/m$. Data for $K_xMn_yCo_{1-y}O_2$ (Figure 1b, Figure S1b) could be indexed to a hexagonal unit-cell with lattice parameters a = 2.88166(7) Å and c = 19.1927(6) Å and space group symmetry $R\bar{3}m$. These unit-cells are similar to those previously reported for monoclinic P'3-type $K_{0.5}MnO_2$[15] and hexagonal P3-type $K_{0.5}MnO_2$.[18] In the P3-type layered structure, oxygen ions are stacked in an ABBCCA sequence along the [001] direction, and each layer is alternatively occupied by octahedrally coordinated $Mn^{3+/4+}$ and prismatically coordinated K^+. The P'3-type monoclinic structure is a distortion of the P3-type hexagonal one in which MnO_6 octahedra deform due to strong Jahn-Teller effects from Mn^{3+} (d^4 electronic configuration).[15] In the monoclinic setting (smallest β angle) used throughout this work, the monoclinic and hexagonal unit-cells are related:

$$\vec{a}_{mon} = 2\vec{a}_{hex} + \vec{b}_{hex}$$
$$\vec{b}_{mon} = \vec{b}_{hex}$$
$$\vec{c}_{mon} = -{}^{2}/_{3}\,\vec{a}_{hex} - {}^{1}/_{3}\,\vec{b}_{hex} + {}^{1}/_{3}\,\vec{c}_{hex}$$

Reflections arising from the impurity phase K_2CO_3[29] are observed in the NPD data for both samples and reflections arising from orthorhombic P2-type $K_{0.51}Mn_{0.94}O_2$[5] are observed only in NPD data of the cobalt-doped sample. The presence of secondary P2-type K_xMnO_2 phase has previously been reported in P3-type $K_{0.5}MnO_2$ samples[18] and visual comparison between XRPD data of this and our work suggests improved purity of our material, noting also the increased sensitivity of NPD toward K_2CO_3 (Figure S1a, b).

The K/M (M = Mn + Co) ratio determined from inductively-coupled plasma – optical emission spectroscopy (ICP-OES) for the as-synthesised materials is ~ 0.5, which is close to that expected, noting that due to the presence of K_2CO_3 the K content of the layered oxide is unknown. As potassium carbonate readily dissolves in water, ICP-OES was repeated for the powders washed with water and the K/M ratio was determined to be ~ 0.3, consistent with that determined from energy-dispersive X-ray (EDX) spectroscopy (Figure S2a, b). The Mn:Co determined from EDX spectroscopy is close to 0.95:0.05 in the doped sample, suggesting $K_{0.3}MnO_2$ and $K_{0.3}Mn_{0.95}Co_{0.05}O_2$ compositions for the two samples. X-ray photoemission spectroscopy (XPS) (Figure S2c, d, e) was used to identify the surface chemical composition and the related valence states of Mn and Co. The peaks at 653.8 and 642.0 eV are assigned to Mn $2p_{3/2}$ and Mn $2p_{1/2}$, respectively. The Mn^{3+}:Mn^{4+} in $K_{0.3}MnO_2$ is found to be ~ 0.3:0.7, while that in $K_{0.3}Mn_{0.95}Co_{0.05}O_2$ is ~ 0.25:0.7, which further confirms the K content in the layered phase as 0.3. As the washing procedure was found to severely affect the crystallinity of the layered phase due to water intercalation and the structure is not fully recovered after drying, no washing of the samples was performed for other

measurements (Figure S3), with *in operando* diffraction measurements confirming the inactivity of impurity phases during cycling.

The crystal structure of $K_{0.3}MnO_2$ and $K_{0.3}Mn_{0.95}Co_{0.05}O_2$ were refined using joint Rietveld refinement against NPD and XRPD data. Refined atomic coordinates are given in Table S1 and S2 and representations of refined structures are given in Figure 1a and b. The refined mass ratio of crystalline phases yields a composition of 86.7 wt.% $K_{0.3}MnO_2$ and 13.3 wt.% K_2CO_3 for the pristine sample and 86.6 wt.% $K_{0.3}Mn_{0.95}Co_{0.05}O_2$, 7.5 wt.% K_2CO_3 and 5.9 wt.% $K_{0.51}M_{0.94}O_2$ for the cobalt-doped sample. The total K/M (M = Mn + Co) atomic ratio of the as-synthesised powder is close to 0.5, corresponding to that estimated from ICP-OES and confirming the estimated composition to be $K_{0.3}MO_2$.

The results confirm the P'3 and P3 stacking organization in the pristine and Co-doped material, respectively, with K^+ occupying prismatic sites of the interlayer in both materials. In monoclinic $K_{0.3}MnO_2$, the MnO_6 octahedra have two elongated opposite bonds (D_{4h} point group) along the [502] direction of the monoclinic lattice, whereas those in hexagonal $K_{0.3}Mn_{0.95}Co_{0.05}O_2$ have equal bond lengths. Refined Mn-O distances are 4 × 1.9181(11) Å and 2 × 2.086(17) Å in $K_{0.3}MnO_2$, and 6 × 1.9401(5) Å in $K_{0.3}Mn_{0.95}Co_{0.05}O_2$. These values are close to those calculated from distances reported (Table S3). For $K_{0.3}MnO_2$, the refinement figures of merit improved upon the introduction of anisotropic displacement parameters for the oxygen; the displacement is largest along the longer M-O bonds (Figure S4a), likely as a result of the mixed occupation of Mn^{3+} and Mn^{4+} at transition metal sites. On the other hand, the refinement of anisotropic displacement parameters for $K_{0.3}Mn_{0.95}Co_{0.05}O_2$ did not improve the figures of merit.

The cooperative Jahn-Teller distortion of MnO_6 octahedra is responsible for the monoclinic symmetry of $K_{0.3}MnO_2$ as the directionality of the deformation results in an *a/b* ratio (1.80 Å) larger than the ideal value $\sqrt{3}$ for a pristine hexagonal lattice. The substitution

of Mn by Co results in the suppression of the cooperative Jahn-Teller distortion in $K_{0.3}Mn_{0.95}Co_{0.05}O_2$. Although Mn-O distances in $K_{0.3}Mn_{0.95}Co_{0.05}O_2$ are constant at long-range, calculated distances suggest that Jahn-Teller active Mn^{3+} is present, but that distortions are not cooperative (Figure S 4b). The suppression of the cooperative effect is probably the result of 1) a smaller amount of Mn^{3+} as the Co^{4+}/Co^{3+} redox couple is more oxidising than Mn^{4+}/Mn^{3+}, and 2) increased disorder at the transition metal site from the random mixing of Co and Mn.

The distortion also extends to KO_6 prisms which are more distorted in $K_{0.3}MnO_2$ than in the cobalt-doped sample. Average refined K-O bond lengths (2.76(2) Å in $K_{0.3}MnO_2$ and 2.760(5) Å in $K_{0.3}Mn_{0.95}Co_{0.05}O_2$) are close to those usually observed in other ionic compounds (2.76 Å).[30] No superstructure reflections appear in powder diffraction data, suggesting that all prismatic sites of the interlayer are crystallographically equivalent. This corresponds to a statistical occupation of 15% by K. This does not preclude the existence of ordering at short-range, to minimize K^+-K^+ repulsions for example due to the close proximity of neighboring prismatic sites. The large refined value for the isotropic atomic displacement parameter of K may arise from local positional disorder and/or ionic mobility within the interlayer.

From the refined unit-cells, the distance between two layers is 6.40 Å in both $K_{0.3}MnO_2$ and $K_{0.3}Mn_{0.95}Co_{0.05}O_2$, which suggests a smaller amount of potassium than previously reported for the P3-type $K_{0.5}MnO_2$ material (6.36 Å).[18] The interplanar distance is confirmed using scanning transmission electron microscopy (STEM) that shows clear lattice fringes between (001) planes (Figure 1c and Figure S5a). Combined STEM with EDX spectroscopy mapping shows that elements are uniformly distributed in the layered oxide phase. The grain morphology of as-synthesized samples was investigated using scanning electron microscopy

(SEM), and both $K_{0.3}Mn_{0.95}Co_{0.05}O_2$ (Figure 1d) and $K_{0.3}MnO_2$ (Figure S5b) are found to possess irregularly shaped submicron particles (between 200 and 500 nm).

Electrochemical measurements were first performed over the voltage window 1.5-3.9 V (Figure S6). The capacity at 22 mA g^{-1} is 132 mA h g^{-1} and 97 mA h g^{-1} (Figure S6c-d) for $K_xMn_{0.95}Co_{0.05}O_2$ and K_xMnO_2, respectively. However, the cycling is not completely reversible, as evidenced by the non-overlapping initial and subsequent cyclic voltammetry (CV) profiles (Figure S6a-b), and results in fast capacity fade, with ~ 50% capacity remaining after 30 cycles for both $K_{0.3}Mn_{0.95}Co_{0.05}O_2$ and $K_{0.3}MnO_2$ (Figure S6e). This capacity fade is similar to that observed for hexagonal P3-type $K_{0.5}MnO_2$,[18] involving a phase transformation that is partially irreversible at high voltage. This phase transformation is the formation of the phase "X" described in the *in operando* SXRPD section, associated with the cathodic peak at ~ 3.8 V and anodic peak at ~ 3.5 V of the CV (Figure S6a-b) that contributes significantly to the capacity.

Although the capacity of $K_{0.3}MnO_2$ is slightly smaller, better long-term performance is obtained when cycling in the restricted voltage range 2.0-3.6 V. The CV and galvanostatic cycling (GC) profiles obtained in this range for $K_{0.3}Mn_{0.95}Co_{0.05}O_2$ and $K_{0.3}MnO_2$ are shown in Figure 2a, 2b and 2c. We note inconsistencies in the profiles during the first five or so cycles between different batteries, with the performance stabilizing afterwards. This could be attributed to many factors such as instability of the newly formed solid electrolyte interphase (SEI) film, where the electrolyte was not optimized for the K-ion chemistry. Spontaneous reduction of the electrode material before cycling was demonstrated by *in situ* XRPD (Figure S7). Nevertheless, the cycling eventually stabilizes and the coulombic efficiency is close to 100.1% and 99.6% for $K_{0.3}Mn_{0.95}Co_{0.05}O_2$ and $K_{0.3}MnO_2$, respectively.

The overlap of the curves between subsequent cycles indicates good reversibility of the processes in the 2.0-3.6 V range. The charge and discharge profiles show significant

polarization, with corresponding cathodic and anodic peaks separated by 0.17-0.20 V in $K_{0.3}Mn_{0.95}Co_{0.05}O_2$ and by 0.22-0.27 V in $K_{0.3}MnO_2$ (Figure 2a). Reversible capacities of 99 and 77 mA h g^{-1} were measured at a current density of 22 mA g^{-1} in the 2.0-3.6 V range, which correspond to the insertion/extraction of 0.37 and 0.29 K^+ in $K_xMn_{0.95}Co_{0.05}O_2$ and K_xMnO_2, respectively (Figure 2b and Figure 2c). The capacity improvement achieved by doping is therefore ~ 30%, and the enhanced capacity is retained over repeated cycling (Figure 2d). The rate performance also improves with doping (Figure 2e and Figure S8a and b), with a smaller capacity decrease in $K_xMn_{0.95}Co_{0.05}O_2$ (~ 45%) compared with K_xMnO_2 (~ 64%) when the current density is increased from 22 to 440 mA g^{-1}. Although a contribution to the capacity may be expected to arise from double layer capacitance when cycled at 173 mA g^{-1}, cyclic voltammetry shows that most of the capacity arises from intercalation processes even at higher scan rates (Figure S8c and d). Long-term cyclability was investigated at the current density of 173 mA g^{-1} (Figure 2f). After 500 cycles, the capacity retention is about 75% of the initial capacity in $K_{0.3}Mn_{0.95}Co_{0.05}O_2$ and about 80% in $K_{0.3}MnO_2$. Both $K_{0.3}Mn_{0.95}Co_{0.05}O_2$ and $K_{0.3}MnO_2$ exhibit coulombic efficiencies over 99.5%. XRPD data and STEM images (Figure S9) of electrodes recovered from coin cells after 100 cycles at 173 mA g^{-1} between 2.0 and 3.6 V confirm that the layered material is stable in this voltage range.

The variations of potential E *vs.* K^+/K obtained from the CV and GC are directly related to the phase transitions that occur in the K_xMO_2 electrode in the half-cell configuration.[31] Although only 5% cobalt replaces manganese, the dissimilar profiles between the pristine and doped samples shows that structural transitions are notably affected by the doping. The mechanism of intercalation was investigated using *in operando* synchrotron X-ray powder diffraction (SXRPD) using customized coin cells containing either $K_{0.3}MnO_2$ or $K_{0.3}Mn_{0.95}Co_{0.05}O_2$. Comparison of *in operando* SXRPD data at the start of cycling with

XRPD data of the precursor materials indicated that both samples spontaneously undergo a chemical reaction in the absence of current within the battery (Figure S7). For $K_{0.3}MnO_2$, the structure of the initial phase is recovered at a lower state-of-charge (Figure S7a), indicating that potassium is intercalated during the initial reaction (spontaneous reduction). Accordingly, the open-circuit voltage of freshly assembled batteries decreases over time before cycling (Figure S10). For $K_{0.3}Mn_{0.95}Co_{0.05}O_2$, its hexagonal structure becomes monoclinic in the electrochemical cell before cycling, which points to reduction as Jahn-Teller distorted Mn^{3+} increases the stability of the monoclinic lattice. The monoclinic structure is maintained at all subsequent states-of-charge and the hexagonal symmetry never recovered. This suggests that either the monoclinic or hexagonal structure at x = 0.3 is metastable at room-temperature. In other layered oxides adopting the monoclinic P'3-type structure at room-temperature, the lattice becomes hexagonal upon heating and the reaction is fully reversible on cooling,[32-33] suggesting a higher stability of the monoclinic form.

A contour plot of the *in operando* SXRPD data during the first discharge and second charge for $K_{0.3}MnO_2$ and $K_{0.3}Mn_{0.95}Co_{0.05}O_2$ are shown in Figure 3 alongside the experimentally measured galvanostatic potential curve at 22 mA g^{-1}. The starting composition K_xMO_2 (M = Co + Mn) of the electrode is not clear due to the self-discharge reaction that occurs before cycling, and the phase composition during cycling were calculated based on an assumed starting formula of $K_{0.3}MO_2$.

In operando SXRPD data for both compounds were successfully indexed to a monoclinic unit-cell at all states-of-charge (Figure 3). Despite the overlap of the 201 and -112 reflections at x > 0.25 and of the 200 and 110 reflections at x < 0.15, other reflections clearly show the monoclinic splitting. In the case of $K_{0.3}Mn_{0.95}Co_{0.05}O_2$, reflections including the 110 and -202 display very low intensity. Reflections arising from other crystalline phases such as the aluminum current collector, the metallic potassium counter electrode, and the K_2CO_3

impurity phase are also visible in the SXRPD data. The position and intensity of K_2CO_3 reflections remained constant during cycling, indicating the electrochemical inactivity of this impurity phase. No reflections arising from the P2-type $K_{0.51}Mn_{0.94}O_2$ were visible in the *in operando* SXRPD data. The elevated background between 18 and 20° arises from the glass separator.

A series of structural transitions of the K_xMO_2 electrode can be identified in the *in operando* SXRPD data and correlated with the voltage variation, with constant voltage observed during two-phase transitions and continuous voltage variation observed during single-phase steps, in agreement with theory.[31] In $K_{0.3}MnO_2$, 4 single-phase steps during discharge and 5 during charge can be identified, whereas in $K_xMn_{0.95}Co_{0.05}O_2$, 5 steps can be seen during discharge and 6 during charge. Each single-phase step is separated by a two-phase transformation. The similarity of the galvanostatic dV/dt and cyclic voltammetry curves allow the assignment of redox peaks to phase transitions (Figure S11). The deducted phase diagram is illustrated in Figure 3. The increased number of two-phase transitions, as well as larger overall volume change (Figure S12), for the doped sample may be responsible for the faster rate of capacity fading after repeated cycling (Figure 2f) although the overall capacity is still higher after 500 cycles.

Unit-cell parameters were determined at most states-of-charge using Le Bail profile matching, with the exclusion of two-phase regions due to significant reflection overlap. The refined unit-cell parameters are given in Table S4 and 5 and plotted in Figure S13, with derived distances $c\cdot\sin\beta$ and a/b given in Figure 4a and b.

The interlayer distance, given by $c\cdot\sin\beta$, decreases at higher K content due to increased interlayer attractive bonding between K^+ and O^{2-}. The size of the triangular lattice, given by averaging $a/\sqrt{3}$ and b, increases with K content due to decreased valence of the transition metal ions from +4 to +3 which lengthens the Mn-O (Co-O) bond distance. The ratio a/b is

equal to $\sqrt{3}$ in a regular hexagonal lattice and deviates from this ideal value in the monoclinic lattice due to distortions induced by cooperative Jahn-Teller effects. Accordingly, the ratio *a/b* deviates from this ideal value as the K content increases as a result of increased Mn^{3+}.

The lower *a/b* ratio of $K_xMn_{0.95}Co_{0.05}O_2$ phases compared with K_xMnO_2 phases confirms that cooperative Jahn-Teller distortions are reduced in the doped sample, enabling more isotropic migration pathways within the (a, b) plane which results in a higher ionic diffusion rate of K^+, as confirmed by GITT measurements (Figure S14), and consistent with the better rate performance and lower polarization (Figure 2) observed for $K_{0.3}Mn_{0.95}Co_{0.05}O_2$. The reduced MO_2 layer distortion is also expected to improve the electronic conductivity of the material, in a similar manner to that observed for $Na_xNi_{1-y}Co_yO_2$.[34]

In sodium layered oxides, phase changes during cycling are usually attributed to alkali ion/vacancy ordering or phase transitions involving the gliding of metal oxygen planes.[35] In K_xMO_2 (M = Mn + Co), no extra reflections arising from potassium ordering could be observed, suggesting that the prismatic sites of the interlayer are crystallographically equivalent although the intensity of superstructure reflections may have been too weak to be seen using *in operando* data. Nevertheless, it is possible to distinguish between the O'3 and P'3-type layered structures from relative peak intensities. The two structures are related by a gliding of the layers along the [100], [130], or [-130] direction that results in distinctly different coordination environments for K: prisms in P'3 and octahedra in O'3. In the monoclinic setting, an O'3 structure will produce intense -202 and 111 reflections and almost absent -112 and 201 reflections, with the opposite occurring for the P'3 structure type. The *in operando* SXRPD data show that both $K_{0.3}MnO_2$ and $K_{0.3}Mn_{0.95}Co_{0.05}O_2$ electrodes initially have the P'3-type structure and reversibly transform into the O'3-type structure at low potassium content, with the transition occurring at $x \approx 0.15$ for $K_{0.3}MnO_2$ and $x \approx 0.12$ for $K_{0.3}Mn_{0.95}Co_{0.05}O_2$. Transformation to the O3-type structure was also observed for the related

hexagonal P3-type K_xMnO_2 material, and density functional theory-based calculations suggested a higher stability of the octahedral coordination at low K content.[18] This result is in contrast with most sodium layered oxides for which the octahedral coordination is usually favored at high alkali content ($x > 0.7$ in Na_xMO_2) and prismatic coordination is favored at lower alkali content,[36,37] however, very low sodium content is rarely achieved due to irreversible transformations that usually occur for compositions with $x < 0.3$. Among the sodium layered oxides with $x < 0.2$, a range of structures have been reported including faulted P3-type $Na_0Ni_{1/2}Mn_{1/2}O_2$[38] and rock-salt structured Na_0CrO_2.[39] Our SXRPD data reveal a phase transition involving layer gliding at $x \approx 0.22$ for K_xMnO_2 and at $x \approx 0.26$ for $K_xMn_{0.95}Co_{0.05}O_2$. In this transformation, the P'3-type structure is maintained but the angle β changes significantly (Figure S13d, h), from 103° (structure is denoted P'3-a type) to 108° (denoted P'3-b type), which is characteristic of layer gliding. For $K_{0.3}Mn_{0.95}Co_{0.05}O_2$, the transition also marks a break in the general trend in the evolution of interlayer distance. As MnO_6 octahedral distortion increases at higher K content, gliding allows conservation of remaining undistorted KO_6 units, with the transition in the β angle likely the result of strain relaxation. The series of glide transitions identified in monoclinic K_xMO_2 (M = Mn + Co) are summarized in Figure 4c.

On the whole, both electrodes undergo reversible transitions during charge and discharge, however, asymmetry is clearly visible. The interlayer distance (Figure 4a and b) decreases after the P'3-type to O'3-type structure transition during charge, as would be expected from the reduced oxygen ion repulsion in the O'3-type (staggered O^{2-}) compared to the P'3-type (stacked O^{2-}) structure, however, this distance remains constant during the transformation on discharge. The interlayer distance in the P'3-type structure is also always smaller during discharge than charge. Incomplete conversion between the P'3-type and O'3-type structures at room temperature has been previously noted,[32] and a similar effect may occur for K_xMO_2.

Such an incomplete conversion is evidenced by the slightly broader P'3-type phase -11*l* reflections in the SXRPD data during discharge (Figure 3). Moreover, increased disorder of P'3-type phase is also consistent with the smoother transformations observed on discharge, with continuous single-phase transformations at x ≈ 0.30 in K_xMnO_2 and x ≈ 0.28 in $K_xMn_{0.95}Co_{0.05}O_2$ (Figure 3 and 4), as opposed to the two-phase reactions during charge. In contrast, the unit-cell parameters for the O'3-type structure are similar during both charge and discharge (Figure 4). Therefore, the cycling is reversible despite the asymmetrical conversion as the material reverts to the same structure at lower K content.

At high potassium content (x > 0.35) the 110, -111 and -112 K_xMnO_2 and $K_xMn_{0.95}Co_{0.05}O_2$ reflections (Figure 3), as well as most higher order reflections, become progressively broader as more potassium is inserted. This could correspond to the formation of faults in the layered structure,[41] however, such faults cannot be reliably determined from the *in operando* SXRPD data. The CV and GC curves (Figure S6) do not point to a two-phase transformation at these potassium levels, suggesting a progressive increase of defects in a reversible process. Even though the crystal structure can theoretically accommodate more K^+, the maximum amount of potassium that can be intercalated in monoclinic K_xMO_2 (M =Mn + Co) is close to x ≈ 0.4. The reversible composition range commonly decreases with the radius of the alkali metal in layered oxides,[8] and difficulty in reaching higher alkali content may arise from stronger interaction between K^+ ions due to the larger interlayer spacing and the closer proximity of electron clouds. According to the crystal radius of six-coordinate K^+ (1.52 Å),[30] adjacent K would overlap in a hypothetical KMO_2 compound when the *b* unit-cell parameter is smaller than 3.04 Å. This imposes a limit on the number of available positions for potassium in the triangular lattice which could be responsible for the observed disorder at x > 0.35.

In operando SXRPD data of $K_{0.3}MnO_2$ batteries during cycling was also performed over the extended voltage range 1.5-4.0 V (Figure S15). As consistent with the CV and GC curve profiles (Figure S6), a two-phase reaction occurs between 3.5 and 3.8 V, with the reflections of $K_{\sim0.04}MnO_2$ fading while a new phase "X" is formed. The first intense reflection of this phase is observed at a d-spacing of ~ 6.49 Å, close to the interlayer distance in $K_{\sim0.04}MnO_2$, however, further indexation was not possible due to the broadening of all other reflections. A similar observation was made for hexagonal P3-type K_xMnO_2 and the so-called "X" phase could not be identified.[18] The transformation is partially reversible, however, the layered structure disappears after several cycles (Figure S15). The loss of the layered structure is probably responsible for the irreversible loss of capacity when cycling in the 1.5-4.0 V range. All reflections become broad in this voltage region, suggesting a high degree of disorder in the resulting material. Local structure characterization may assist with the identification of the new phase formed.

In conclusion, a comprehensive study of the electrochemical properties and structural phase evolution during cycling of monoclinic $K_{0.3}MnO_2$ and $K_{0.3}Mn_{0.95}Co_{0.05}O_2$ is presented. Notably, this work reveals the suppression of cooperative Jahn-Teller distortion induced by Mn^{3+} as a result of cobalt doping, leading to a more isotropic migration pathway for K^+ in the interlayer. This enhances both the K^+ diffusion rate and the rate performance, with $K_{0.3}Mn_{0.95}Co_{0.05}O_2$ delivering a reversible capacity of 99 mA h g^{-1} at 22 mA g^{-1} in the voltage window 2.0-3.6 V, compared with 77.1 mA h.g^{-1} for the pristine $K_{0.3}MnO_2$ material, and a 92% higher reversible capacity at 440 mA g^{-1} for the Co doped material. This work therefore demonstrates that cobalt-doped K_xMnO_2 can be regarded as a suitable candidate positive electrode material for potassium ion batteries.

Some issues remain regarding the stability of the layered oxide material, and although the capacity after 500 cycles remains higher in the cobalt doped compared with pristine material,

the capacity decay is enhanced, reducing after 500 cycles from 83% to 74% of its initial value. Detailed insights into the mechanism of this structural instability are provided by our *in operando* powder diffraction study. Phase transitions that involve layer gliding were identified in both pristine and cobalt-doped samples, with an asymmetry observed between charge and discharge that may arise from incomplete gliding between the P'3-type and O'3-type structures. We find that the reversible capacity of the cobalt doped sample is limited to 0.4 K per MO_2 (M = Mn + Co), where structural faults are introduced at high potassium content, probably due to the relatively large size K^+ that prevents close-packing within the interlayer. This suggests that capacity may be increased further by substitution with elements possessing larger radii (*e.g.* 4*d*-5*d* transition metals and/or S or Se anions) that would result in increased distances in the (001) plane. Cycling at voltages larger than 3.6 V resulted in fast capacity fade due to the irreversible loss of the layered phase at high voltage.

Considering the relationship between electrochemical performance and crystal structure, the relatively moderate 5% cobalt doping effectively promoted the material's rate capability by providing more isotropic migration pathways for K^+ in the interlayer, yet inevitably impairing cyclability by triggering additional phase transitions upon cycling. We hope that these mechanistic insights will motivate the further improvement of this material in the future, with the doping level yet to be optimized. The high toxicity of cobalt also motivates the future exploration of safer and potentially cost-effective alternative dopants in this material, noting that cobalt is used extensively in many commercial LIB electrodes. Inspired by the ternary materials that successfully led LIB and SIB development, a prospective strategy for designing high-performance PIB electrodes may lie in the introduction of another inactive metal ion such as Mg^{2+}, Zn^{2+}, Ni^{3+}, or Cr^{3+}, to further stabilize the structure.[42-47] Further, the minor stability issues of this electrode may be overcome through optimisation, such as was achieved for graphitic electrodes used in LIBs which exhibited relatively large

instability in the early stages of the technology.[48] The current study provides a fundamental understanding of the mechanism of K intercalation in layered oxides, informing the strategic development of these materials for use in PIBs.

Supporting Information
Supporting Information is available from the Wiley Online Library or from the author.

Acknowledgements
Q.Z. and C.D. contributed equally to this work. Financial support provided by the Australian Research Council (ARC) (FT150100109, FT160100251, LP160101629, DP170102406 and LE180100141) is gratefully acknowledged. The scholarship for Q.Z. is supported by the China Scholarship Council (CSC, Grant No. 201508420150). The work contains experiments conducted at the powder diffraction beamline of the Australian Synchrotron and at the Australian Centre for Neutron Scattering. The authors also gratefully acknowledge assistance by Dr. Qinfeng Gu and Dr. Helen Brand at the Powder Diffraction beamline of the Australian Synchrotron, Dr. Gilberto Casillas-Garcia at the Electron Microscopy Centre of the University of Wollongong for STEM measurements.

Received: ((will be filled in by the editorial staff))
Revised: ((will be filled in by the editorial staff))
Published online: ((will be filled in by the editorial staff))

References

[1] Z. L. Jian, W. Luo, X. L. Ji, *J. Am. Chem. Soc.* **2015**, 137, 11566-11569.

[2] S. Komaba, T. Hasegawa, M. Dahbi, K. Kubota, *Electrochem. Commun.* **2015**, 60, 172-175.

[3] J. C. Pramudita, D. Sehrawat, D. Goonetilleke, N. Sharma, *Adv. Energy. Mater.* **2017**, 7, 1602911.

[4] Q. Zhang, Z. J. Wang, S. L. Zhang, T. F. Zhou, J. F. Mao, Z. P. Guo, *Electrochem. Energy. Rev.* **2018**, 4, 625-658.

[5] Q. Zhang, J. F. Mao, W. K. Pang, T. Zheng, V. Sencadas, Y. Z. Chen, Y. J. Liu, Z. P. Guo, *Adv. Energy. Mater.* **2018**, 8, 1703288; S. K. Chong, Y. F. Wu, C. F. Liu, Y. Z. Chen, S. W. Guo, Y. N. Liu, *Nano Energy* **2018**, 54, 106-115.

[6] Y. J. Liu, Z. X. Tai, J. Zhang, W. K. Pang, Q, Zhang, H. F. Feng, K. Konstantinov, Z. P. Guo, H. K. Liu, *Nature Commun.* **2018**, 9, 3645; H. Gao, T. F. Zhou, Y. Zhang, Q. Zhang, Y. Q. Liu, J. Chen, H. K. Liu, Z. P. Guo, *Adv. Funct. Mater.* **2017**, 27, 1702634.

[7] Z. W. Liu, P. Li, G. Q. Suo, S. Gong, W. Wang, C. Y. Lao, Y. J. Xie, H. Guo, Q. Y. Yu, W. Zhao, K. Han, Q. Wang, M. L. Qin, K. Xi, X. H. Qu, *Energy. Environ. Sci.* **2018**, 11, 3033-3042; B. Cao, Q. Zhang, H. Liu, B. Xu, S. L. Zhang, T. F. Zhou, J. F. Mao, W. K. Pang, Z. P. Guo, A. Li, J. S. Zhou, X. H. Chen, H. H. Song, *Adv. Energy. Mater.* **2018**, 8, 1801149.

[8] Y. Hironaka, K. Kubota, S. Komaba, *Chem. Commun.* **2017**, 53, 3693-3696.

[9] H. Kim, J. C. Kim, S. H. Bo, T. Shi, D. H. Kwon, G. Ceder, *Adv. Energy. Mater.* **2017**, 7, 1700098.

[10] T. Masese, K. Yoshii, Y. Yamaguchi, T. Okumura, Z. D. Huang, M. Kato, K. Kubota, J. Furutani, Y. Orikasa, H. Senoh, H. Sakaebe, M. Shikano, *Nature Commun.* **2018**, 9, 3823.

[11] T. Deng, X. L. Fan, C. Luo, J. Chen, L. Chen, S. Hou, N. Eidson, X. Q. Zhou, C. S. Wang, *Nano Lett.* **2018**, 18, 1522-1529.

[12] J. Y. Hwang, J. Kim, T. Y. Yu, S. T. Myung, Y. K. Sun, *Energy. Environ. Sci.* **2018**, 11, 2821-2827.

[13] L. Q. Deng, X. G. Niu, G. S. Ma, Z. Yang, L. Zeng, Y. J. Zhu, L. Guo, *Adv. Funct. Mater.* **2018**, 28, 1800670.

[14] Y. H. Zhu, Q. Zhang, X. Yang, E. Y. Zhao, T. Sun, X. B. Zhang, S. Wang, X. Q. Yu, J. M. Yan, Q. Jiang, *Chem.* **2019**, 5, 168-179.

[15] C. Delmas, C. *Z.* Fouassier, *anorg. ally. Chem.* **1976**, 420, 184-192.

[16] A. C. Gaillot, V. A. Drits, A. Manceau, B. Lanson, *Micropor. Mesopor. Mater.* **2007**, 98, 267-282.

[17] C. Vaalma, G. A. Giffin, D. Buchholz, S. Passerini, *J. Electrochem. Soc.* **2016**, 163, A1295-A1299.

[18] H. Kim, D. H. Seo, J. C. Kim, S. H. Bo, L. Liu, T. Shi, G. Ceder, *Adv. Mater.* **2017**, 29, 1702480.

[19] A. R. Armstrong, R. Gitzendanner, A. D. Robertson, P. G. Bruce, *Chem. Commun.* **1998**, 1833-1834.

[20] A. R. Armstrong, A. D. Robertson, R. Gitzendanner, P. G. Bruce, *J. Solid State Chem.* **1999**, 145, 549-556.

[21] A. R. Armstrong, A. D. Robertson, P. G. Bruce, *Electrochim. Acta* **1999**, 45, 285-294.

[22] A. D. Robertson, A. R. Armstrong, P. G. Bruce, *Chem. Mater.* **2001**, 13, 2380-2386.

[23] A. I. Landa, C. C. Chang, P. N. Kumta, L. Vitos, I. A. Abrikosov, *Solid State Ionics* **2002**, 149, 209-215.

[24] X. M. Wu, R. X. Li, S. Chen, Z. Q. He, M. F. Xu, *Bull. Mater. Sci.* **2008**, 31, 109-113.

[25] R. J. Clément, J. Billaud, A. R. Armstrong, G. Singh, T. Rojo, P. G. Bruce, C. P. Grey, *Energy. Environ. Sci.* **2016**, 9, 3240-3251.

[26] C. L. Liu, S. H. Luo, H. B. Huang, Z. Y. Wang, A. M. Hao, Y. C. Zhai, Z. W. Wang, *Electrochem. Commun.* **2017**, 82, 150-154.

[27] X. P. Wang, X. M. Xu, C. J. Niu, J. S. Meng, M. Huang, X. Liu, Z. Liu, L. Q. Mai, *Nano Lett.* **2017**, 17, 544-550.

[28] T. Deng, X. L. Fan, J. Chen, L. Chen, C. Luo, X. Q. Zhou, J. H. Yang, S. Y. Zheng, C. S. Wang, *Adv. Funct. Mater.* **2018**, 28, 1800219.

[29] B. M. Gatehouse, D. J. Lloyd, *J. Chem. Soc., Dalton Trans.* **1973**, 70-72.

[30] R. D. Shannon, *Acta Cryst.* **1976**, 32, 751-767.

[31] M. D. Radin, S. Hy, M. Sina, C. C. Fang, H. D. Liu, J. Vinckeviciute, M. H. Zhang, M. S. Whittingham, Y. Meng, A. Ven der Van, *Adv. Energy Mater.* **2017**, 7, 1602888.

[32] C. Didier, M. Guignard, M. R. Suchomel, D. Carlier, J. Darriet, C. Delmas, *Chem. Mater.* **2016**, 28, 1462-1471.

[33] M. Blangero, D. Carlier, M. Pollet, J. Darriet, C. Delmas, J. P. Doumerc, *Phys. Rev. B* **2008**, 77, 184116.

[34] C. Delmas, I. Saadoune, P. Dordor, *Mol. Cryst. Liq. Cryst.* **1994**, 244,337-342.

[35] A. J. Toumar, S. P. Ong, W. D. Richards, S. Dacek, G. Ceder, *Phys. Rev. Appl.* **2015**, 4, 064002.

[36] C. Delmas, J. J. Braconnier, C. Fouassier, P. Hagenmuller, *Solid State Ionics* **1981**, 3/4, 165-169.

[37] A. Mendiboure, C. Delmas, P. Hagenmuller, *J. Solid State Chem.* **1985**, 57, 323-331.

[38] S. Komaba, T. Nakayama, A. Ogata, T. Shimizu, C. Takei, S. Takada, A. Hokura, I. Nakai, *ECS Trans.* **2009**, 16, 43-55.

[39] S. H. Bo, X. Li, A. J. Toumar, G. Ceder, *Chem. Mater.* **2016**, 28, 1419-1429.

[40] J. F. Bérar, P. Lelann, *J. Appl. Cryst.* **1991**, 24, 1-5.

[41] C. Schimpf, M. Motylenko, D. Rafaja, *Mater. Charact.* **2013**, 86, 190-199.

[42] Z. P. Guo, S. Zhong, G. X. Wang, H. K. Liu, S. X. Dou, *J. Alloy. Compd.* **2003**, 348, 231-235.

[43] X. M. Wu, R. X. Li, S. Chen, Z. Q. He, M. F. Xu, *Bull. Mater. Sci.* **2008**, 31, 109-113.

[44] J. Billaud, G. Singh, A. R. Armstrong, E. Gonzalo, V. Roddatis, M. Armand, T. Rojo, P. G. Bruce, *Energy. Environ. Sci.* **2014**, 7, 1387-1391.

[45] Y. You, S. O. Kim, A. Manthiram, *Adv. Energy. Mater.* **2017**, 7, 1601698.

[46] H. R. Yao, P. F. Wang, Y. Wang, X. Q. Yu, Y. X. Yin, Y. G. Guo, *Adv. Energy. Mater.* **2017**, 7, 1700189.

[47] H. Kim, D. H. Seo, A. Urban, J. Lee, D. H. Kwon, S. H. Bo, T. Shi, J. K. Papp, B. D. McCloskey, G. Ceder, *Chem. Mater.* **2018**, 30, 6532-6539.

[48] R. Yazami, P. H. Touzain, *J. Power Sources* **1983**, 9, 365-371.

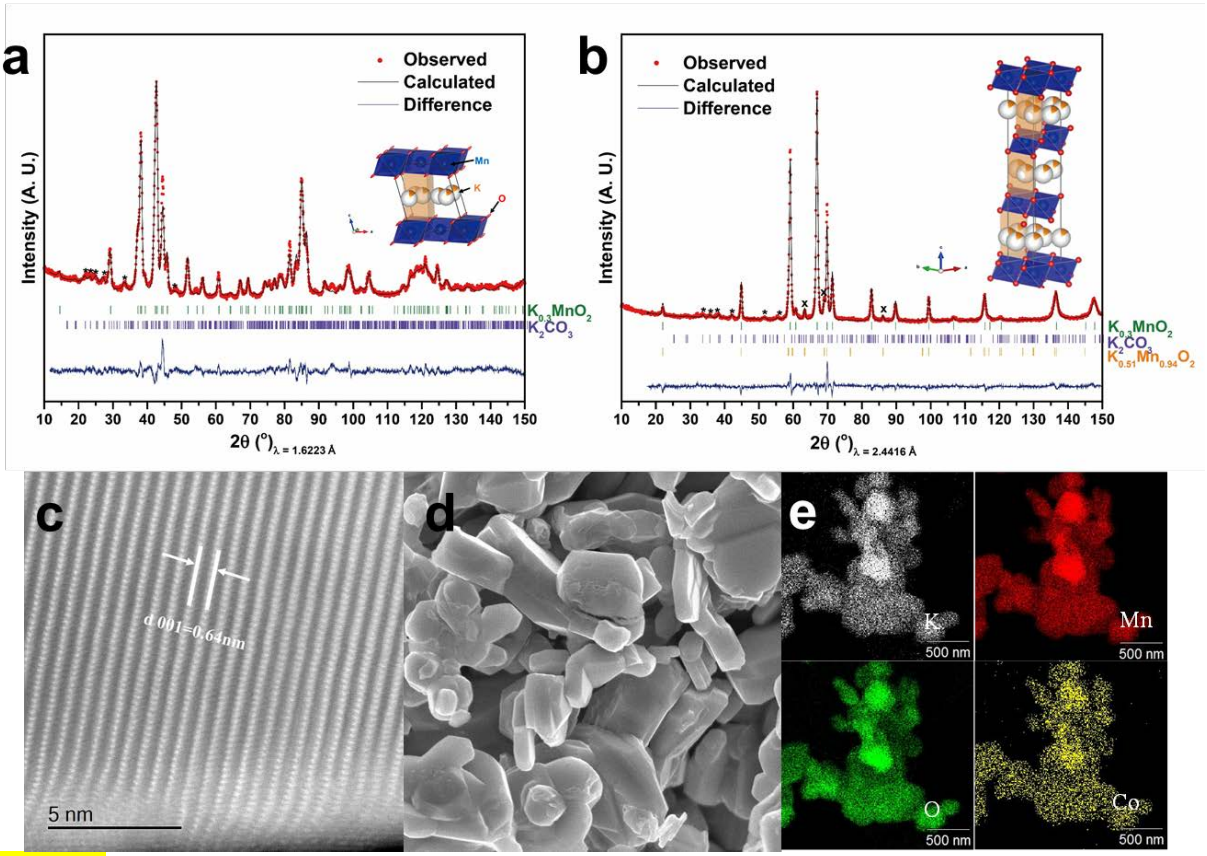

Figure 1. Rietveld refinement profiles using neutron powder diffraction data of as-synthesized a) $K_{0.3}MnO_2$ and b) $K_{0.3}Mn_{0.95}Co_{0.05}O_2$, where vertical lines are reflection markers for each phase and the refined crystal structure of the main phase is shown inset with potassium in orange, manganese in blue, and oxygen in red; c) STEM dark field image of $K_{0.3}Mn_{0.95}Co_{0.05}O_2$ showing (001) planes; d) SEM image of $K_{0.3}Mn_{0.95}Co_{0.05}O_2$ particles; e) Elemental distribution obtained from EDX spectroscopy mapping in $K_{0.3}Mn_{0.95}Co_{0.05}O_2$.

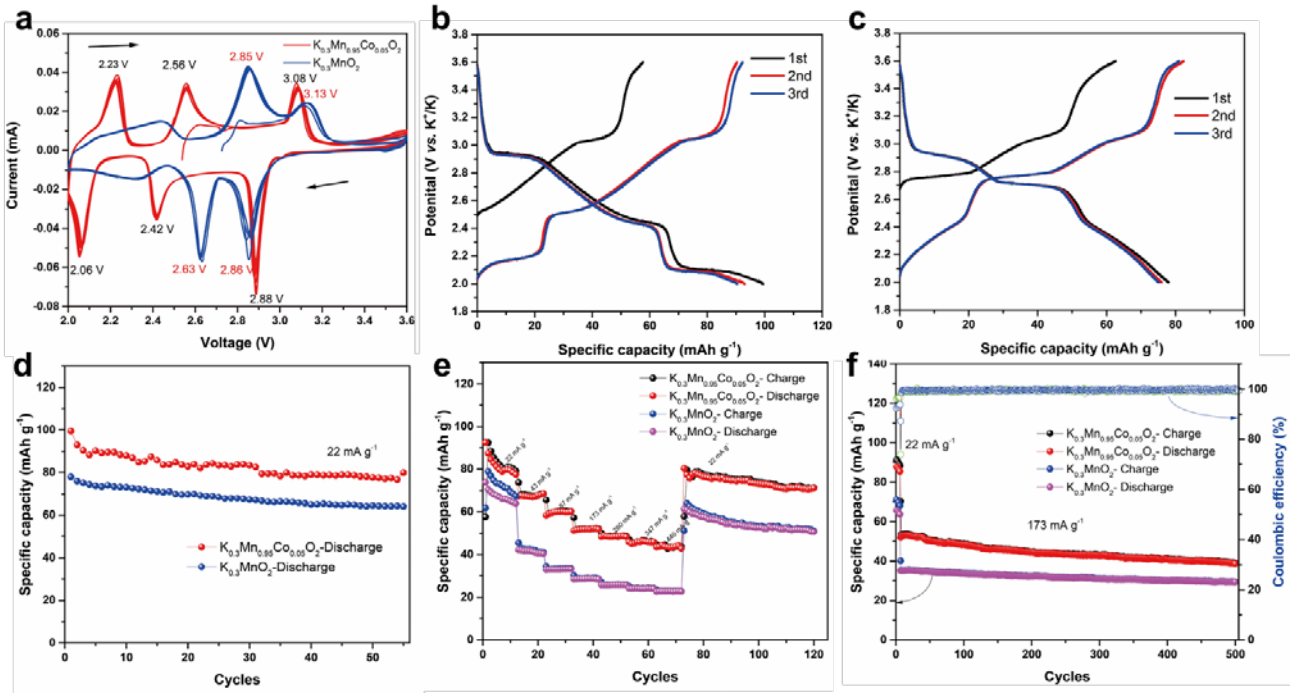

Figure 2. a) Cyclic voltammetry profiles of $K_{0.3}Mn_{0.95}Co_{0.05}O_2$ and $K_{0.3}MnO_2$ vs. K in a half-cell at a scan rate of 0.1 mV.s^{-1}; galvanostatic charge/discharge profiles at 22 mA g^{-1} within the voltage range 2.0-3.6 V for b) $K_{0.3}Mn_{0.95}Co_{0.05}O_2$ and c) $K_{0.3}MnO_2$; d) Specific discharge capacity at 25 mA g^{-1} within the range 2.0-3.6 V; e) Rate performance under current densities of 22, 43, 87, 173, 260, 347, 440 mA g^{-1}; f) Long-term cyclability and coulombic efficiency at a current density of 173 mA g^{-1}. The voltage window is 2.0-3.6 V.

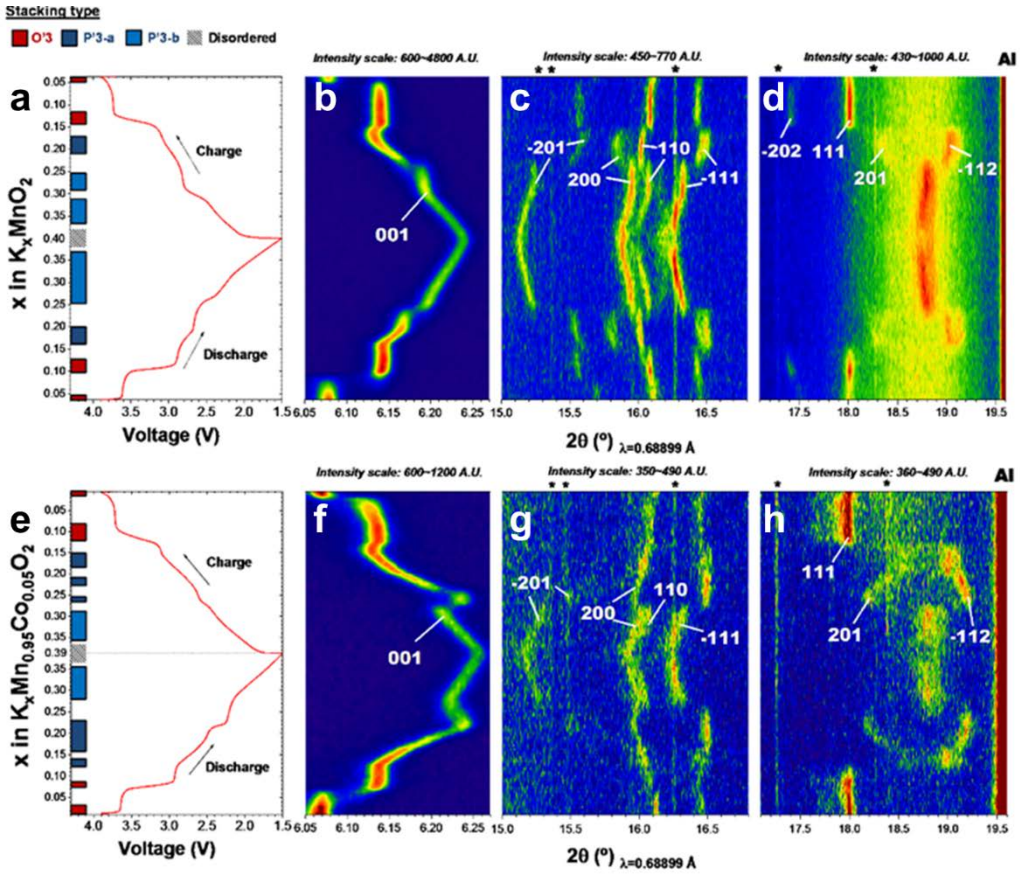

Figure 3. First galvanostatic discharge and second galvanostatic charge (a and b) of batteries containing $K_{0.3}MnO_2$ (top) and $K_{0.3}Mn_{0.95}Co_{0.05}O_2$ (bottom) and their corresponding *in operando* SXRPD data over angular ranges 6.05-6.27° (b and f) 15-16.8° (c and g), and 17.1-19.6° (g and h). Some reflections indexed to the monoclinic lattice are marked. Asterisks identify the position of some K_2CO_3 reflections and the aluminium metal reflection is marked. Associated single layered phases are labelled in the discharge-charge curves and shown in blue for the P'3-type and red for the O'3-type structure, and the hashed block marks reflection broadening observed at higher K content.

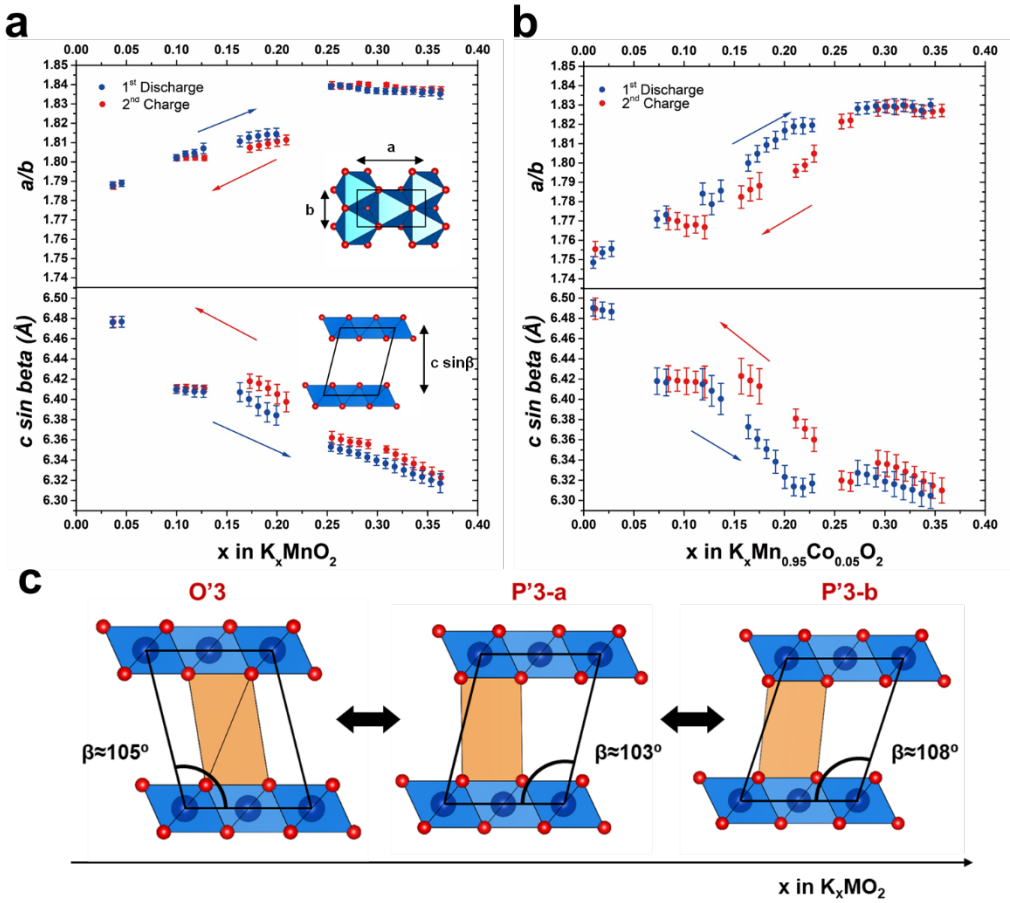

Figure 4. Derived distances obtained from refined unit-cell parameters using *in operando* SXRPD data for a) $K_{0.3}MnO_2$ and b) $K_{0.3}Mn_{0.95}Co_{0.05}O_2$. Gaps in data arise at particular compositions where the presence of multiple layered phases prevented unit-cell refinement. Error bars are the estimated standard deviations as corrected for local correlations after Bérar and Lelann[40]; c) Schematic illustration of the glide transitions in monoclinic K_xMO_2 (M = Mn + Co) with unit-cell parameters of K_xMnO_2 at x ≈ 0.1, 0.2, and 0.35 during charge with the position of oxygen approximated from the expected Mn^{3+}/Mn^{4+} ratio.

The table of contents entry

A reduction of Jahn-Teller distortion at most states-of-charge was achieved *via* 5% cobalt doping on the manganese site in P'3-type K_xMnO_2 layered oxide. As a result, the doped material exhibits significantly improved reversible capacity and diffusion rate of K^+ when used as positive electrode in potassium-ion batteries. *In operando* synchrotron X-ray diffraction revealed the series of phase transformations during cycling, with layer gliding transitions that may affect the long-term stability of the electrode.

Keywords: Potassium Ion Batteries, Cobalt Doping, Rate capability, Cooperative Jahn-Teller Distortions

Qing Zhang, Christophe Didier, Wei Kong Pang, Yajie Liu, Zhijie Wang, Sean Li, Vanessa K. Peterson, Jianfeng Mao* and Zaiping Guo *

Title: Structural insight into layer gliding and Jahn-Teller distortion in layered manganese oxide electrodes for potassium ion batteries

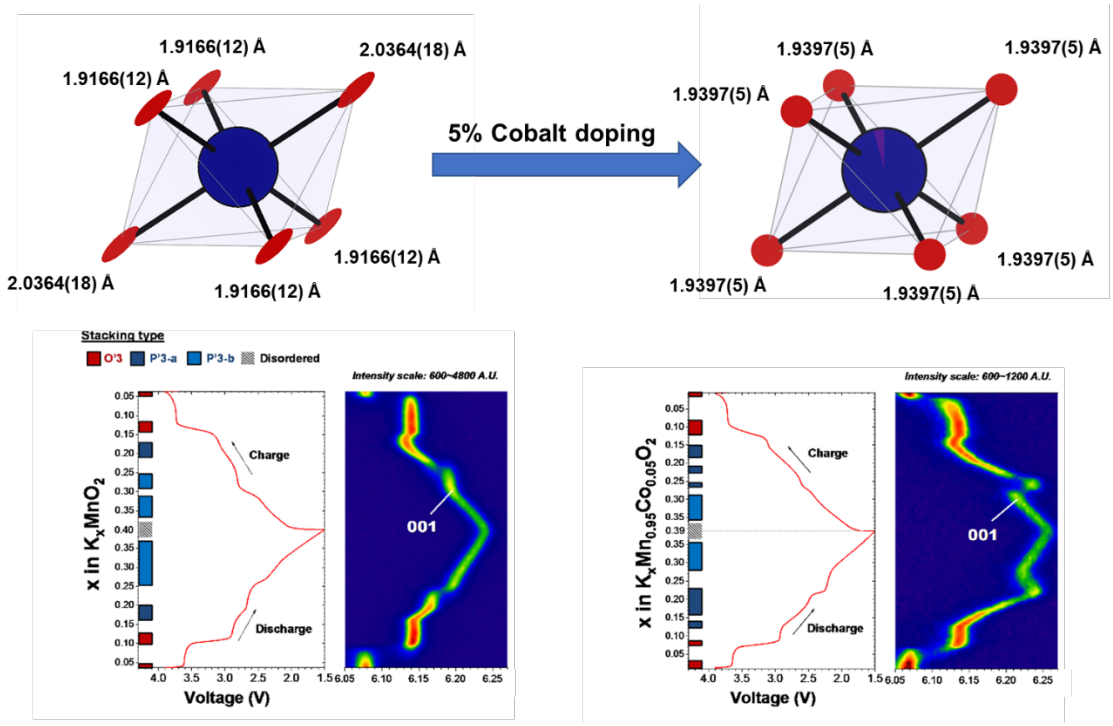

TOC Figure

Supporting Information

Structural insight into layer gliding and lattice distortion in layered manganese oxide electrodes for potassium ion batteries

Qing Zhang, Christophe Didier, Wei Kong Pang, Yajie Liu, Zhijie Wang, Sean Li, Vanessa K. Peterson, Jianfeng Mao and Zaiping Guo **

Qing Zhang, Dr. Christophe Didier, Dr. Wei Kong Pang, Dr. Yajie Liu, Zhijie Wang, Dr. Vanessa K. Peterson, Dr. Jianfeng Mao*, and Prof. Zaiping Guo*
Institute for Superconducting & Electronic Materials, University of Wollongong, Wollongong, NSW 2522, Australia.
E-mail: jmao@uow.edu.au, zguo@uow.edu.au
Dr. Christophe Didier and Prof. Vanessa K. Peterson
Australia Nuclear Science and Technology Organisation, Lucas Heights, NSW 2234, Australia.
Prof. Sean Li
School of Materials Science and Engineering, The University of New South Wales, Kensington, New South Wales 2052, Australia.
Prof. Zaiping Guo and Prof. Vanessa K. Peterson
School of Mechanical, Materials, Mechatronics & Biomedical Engineering, University of Wollongong, NSW 2500, Australia.
Prof. Zaiping Guo
College of Chemistry and Chemical Engineering, Hubei University

Experimental section:

Synthesis of $K_{0.3}MnO_2$ and $K_{0.3}Mn_{0.95}Co_{0.05}O_2$:

The layered oxide materials were synthesized *via* a sol-gel method using KOH (semiconductor grade, pellets, 99.99%, Sigma-Aldrich), $Mn(CH_3COO)_2$•4 H_2O (purum p.a., ≥ 99.0%, Sigma-Aldrich) and $Co(CH_3COO)_2$•4 H_2O (ACS reagent, ≥ 98.0%, Sigma-Aldrich) as precursors with citric acid (ACS reagent, ≥ 99.5%, Sigma-Aldrich) as a chelating agent. For $K_{0.3}MnO_2$, the molar ratio of KOH: $Mn(CH_3COO)_2$•4 H_2O : citric acid was 0.6 : 1 : 10.4 and for $K_{0.3}Mn_{0.95}Co_{0.05}O_2$ the molar ratio of KOH : $Mn(CH_3COO)_2$•4 H_2O : $Co(CH_3COO)_2$•4 H_2O : citric acid was 0.6 : 0.95 : 0.05 : 10.4. All agents were homogeneously mixed with few milliliters of deionized water with the transparent gel that first formed transforming into a semi-solid plaster-like mixture. The resulting mixture was dried in an oven at 150 °C for 3 h and subsequently calcined in a muffle furnace at 600 °C for 2 h, before calcination at 800 °C for 12 h, using a heating rate of 3 °C min^{-1}. The as-prepared product was then cooled to ~200 °C and immediately transferred into an argon-filled glovebox to avoid contamination from moisture in the air.

Material characterization:

Structural characterization of the as-synthesized samples:

For $K_{0.3}MnO_2$, X-ray powder diffraction (XRPD) data were collected on the powder diffraction (PD) beamline at the Australian Synchrotron at the wavelength λ = 0.8275 Å in a 0.3 mm diameter borosilicate capillary.[1, 2] Neutron powder diffraction (NPD) data were collected on the ECHIDNA[3] diffractomer (OPAL, ANSTO) at the wavelength λ = 1.62230(6) Å in a 9 mm vanadium can. For $K_{0.3}Mn_{0.95}Co_{0.05}O_2$, XRPD data were collected on a D8 Bruker diffractometer at the wavelength λ = 1.5406 Å in a 0.2 mm diameter borosilicate capillary and NPD data were collected on the ECHIDNA diffractomer (OPAL, ANSTO) using neutrons with the wavelength λ = 2.44164(10) Å in a 9 mm vanadium can. Phase identification was performed using crystal structures from the ICSD[4] and ICDD[5] databases. Radiation wavelengths at the AS and ECHIDNA instruments were determined using the $La^{11}B_6$ National Institute of Standards and Technology's Standard Reference Material 660b.

Joint Rietveld refinement using the synchrotron X-ray + neutron powder diffraction data were performed using the JANA2006 software.[6] Due to strong correlation between site occupancy and atomic displacement parameters, the site occupancy factor of K was fixed so that the unit-cell formula remained at the $K_{0.3}MO_2$ (M = Mn + Co) composition determined from inductively coupled plasma-optical emission spectroscopy (ICP-OES) measurements performed on water-washed samples. Secondary phases K_2CO_3,[7] as well as the P2-type $K_{0.51}Mn_{0.94}O_2$[8] in the case of the cobalt-doped sample, were included in the phase description of NPD data and their atomic parameters fixed. As these phases contribute only weakly to diffracted intensities they did not interfere with the refinement of the layered phase structure.

Morphological and surface chemical characterization:

Morphological features of the samples were investigated using field-emission scanning electron microscopy (FESEM; JEOL-7500). Atomic-level images and elemental mapping were obtained using a high-resolution scanning transmission electron microscopy (STEM) using energy-dispersive X-ray (EDX) analysis (JEOL JEM-ARM200F, 200kV). X-ray photoelectron spectroscopy (XPS) was conducted on a VG Multilabel 2000, using a vacuum transfer module to prevent moisture exposure.

Electrochemical measurements:

Electrochemical characterization was conducted using CR2032 coin-cells. Working electrodes were prepared by mixing 70 wt.% active material, 20 wt.% carbon black (fine powder, TIMCAL), and 10 wt.% polyvinylpyrrolidone (powder, Sigma-Aldrich) in *N*-Methyl-2-

pyrrolidone (anhydrous, 99.5%, Sigma-Aldrich) to form a slurry. The slurry was then coated onto aluminum foil and dried at 120 °C for 12 h under vacuum to remove residual solvent. The vacuum is maintained until the temperature is below 40 °C and the printed electrode in then pressed under 300 kg.cm^{-2} pressure. The electrode mass loading was about 1.2 g cm^{-2}. Coin cells were assembled in an argon-filled glove box with water and oxygen content below 0.1 ppm. Potassium metal was used as the counter electrode. The electrolyte was 0.8 M KPF_6 dissolved in diethyl carbonate/ethylene carbonate (Sigma-Aldrich, anhydrous ≥ 99.0%, 1:1 v/v). Galvanostatic charge/discharge were carried on a LAND CT2001A tester (China). Cyclic voltammetry (CV) was performed on a Biologic VPM3 electrochemical workstation. All testing was conducted after performing 5 cycles at 22 mA g^{-1}. Measurements were conducted in the voltage range 2.0-3.6 V at 0.1 mV s^{-1} and rate performance was conducted at 22, 43, 87, 173, 260, 347, 440mA g^{-1} in the 2.0-3.6 V voltage range. Long-term cycling tests were conducted at 173 mA g^{-1} (Figure 3f). The weight of inactive impurity phases was excluded in all electrochemical test results.

The galvanostatic intermittent titration technique (GITT) was performed on coin cells containing $K_xMn_{0.95}Co_{0.05}O_2$ and K_xMnO_2 to investigate the diffusion of K^+ in these electrodes. All measured coin cells were activated with a current density of 22 mA g^{-1} 10 times before testing. The electrodes were charge/discharged for 10 min at a pulse current of 22 mA g^{-1} and relaxed for 2 h to approach equilibrium potential. The effective diffusion coefficient (D_{eff}) was calculated for each pulse/relaxation step following the simplified equation derived from Fick's second law[9, 10]:

$$D_{eff} = \frac{4}{\pi\tau}\left(\frac{m_B V_M}{M_B S}\right)^2 \left(\frac{\Delta E_s}{\Delta E_\tau}\right)^2$$

where ΔE_s (V) is the difference between the equilibrium potential before and after the current pulse; ΔE_τ (V) is the difference between the potential under current at the start and end of the current pulse, neglecting ohmic overpotential; τ (s) is the duration of the current pulse; m_B is the mass of the active material in the electrode; V_M and M_B are the molar volume and molar mass of the active material, respectively, V_M/M_B is the reciprocal of the active material density; S is the electrode surface area (cm^2) as reported in the experimental section.

Stability after extended cycling:

To confirm the stability of the material over extended cycling, K_xMnO_2 and $K_xMn_{0.95}Co_{0.05}O_2$ electrodes were recovered from coin cells cycled 100 times at 173 mA g^{-1} within 2.0-3.6 V. The coin cells were disassembled in an Ar-filled glovebox and XRPD was performed on the electrode covered with Kapton tape to prevent exposure to air. Samples for STEM analysis were also prepared in an Ar-filled glovebox and a sample transfer container used to protect the samples from air.

***In operando* X-ray powder diffraction:**

CR2032 coin cells were used for *in operando* synchrotron X-ray powder diffraction measurements with 5 mm diameter holes on each side that were sealed with Kapton tape with an internal component assembly identical to those used for electrochemical measurements. *In operando* X-ray powder diffraction was performed on the PD beamline at the Australian Synchrotron. Data were collected during galvanostatic cycling every 4.7 min at a wavelength 0.68899(5) Å, determined using the $La^{11}B_6$ National Institute of Standards and Technology Standard Reference Material 660b. The galvanostatic charge/discharge was conducted using a battery tester (Neware, China) in the voltage window 1.5-3.9 V.

The relative amount of inserted/removed potassium Δx was calculated using:

$$\Delta Q = I \times \Delta t = \mathcal{F} \times n(K_x MO_2) \times \Delta x$$

Where ΔQ is the change in stored capacity (mA h), I is the applied current (mA), Δt is the time between two states-of-charge (h), F is the Faraday constant (mA h mol^{-1}), $n(K_xMO_2)$ is the amount of layered oxide material (mol), and Δx is the change in embedded potassium, from K_xMnO_2 to $K_{x-\Delta x}MnO_2$ so that I and Δx are positive during charge and negative during discharge. The values given in Figures 3 and 4 were calculated assuming $K_{0.3}MnO_2$ as the starting composition. We note that the actual starting composition of the material before cycling is likely higher due to an unknown amount of self-discharge. We chose not to apply any approximate correction, meaning that compositions may be slightly shifted in x although the relative change of composition Δx is correctly estimated.

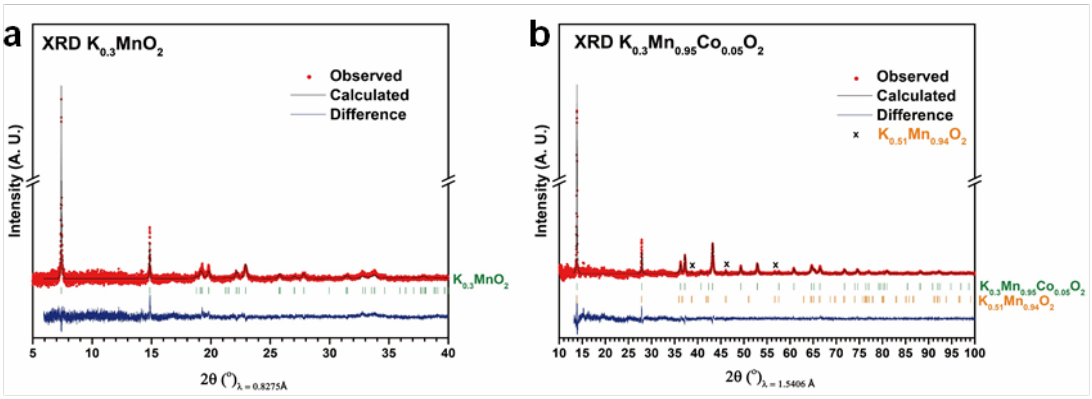

Figure S1 Rietveld refinement profiles using X-ray powder diffraction (XRPD) data of as-synthesised a) $K_{0.3}MnO_2$ and b) $K_{0.3}Mn_{0.95}Co_{0.05}O_2$. For improved clarity the background has been subtracted. Vertical lines are reflection positions for each phase. The K_2CO_3 phase was excluded from the refinement.

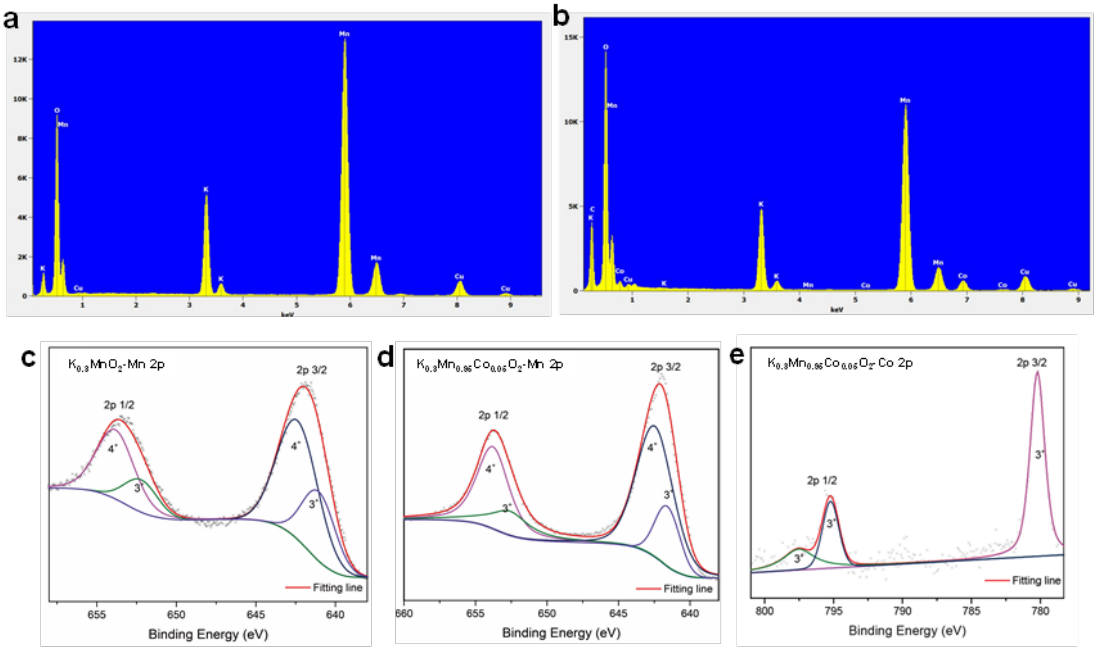

Figure S2 EDX spectrum of as-synthesized a) $K_{0.3}MnO_2$, and b) $K_{0.3}Mn_{0.95}Co_{0.05}O_2$; high-resolution XPS spectrum at the c) Mn 2p edge for $K_{0.3}MnO_2$; d) Mn 2p and e) Co 2p edge for $K_{0.3}Mn_{0.95}Co_{0.05}O_2$.

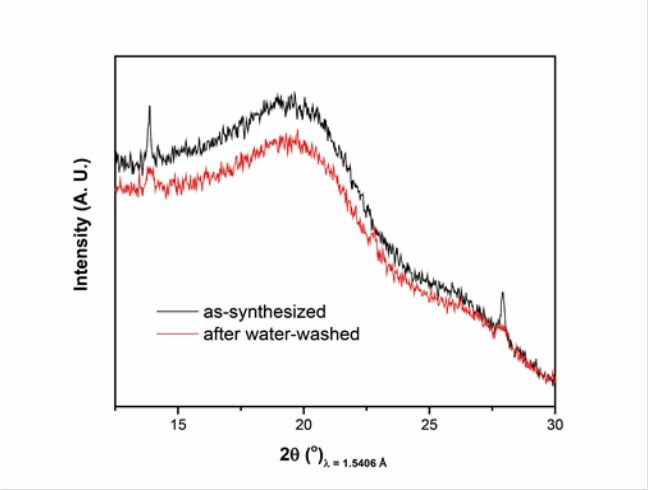

Figure S3 XRPD data of $K_{0.3}MnO_2$ as-synthesized and after washing with water. The broad signal around 20° arises from the Kapton tape used to isolate samples from the air.

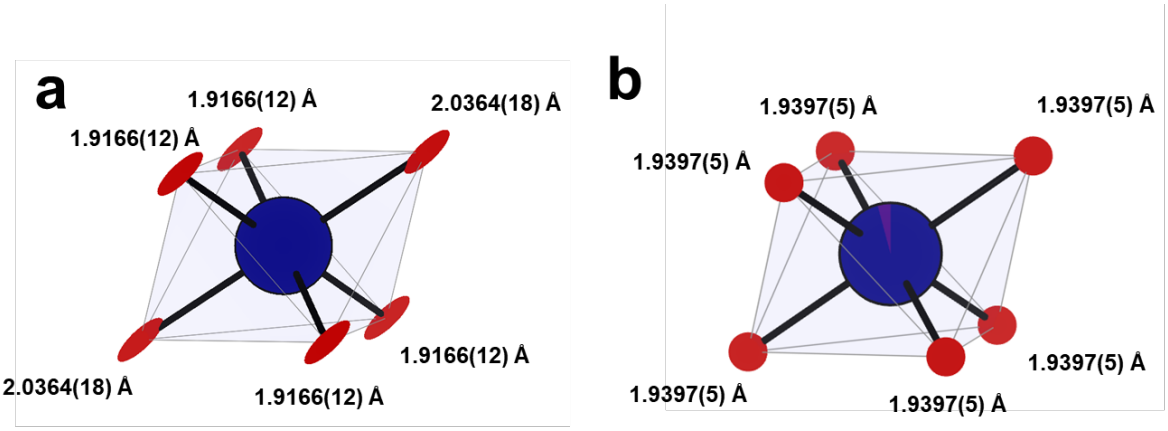

Figure S4 Representation of distorted MnO_6 octahedra in a) $K_{0.3}MnO_2$ and b) $K_{0.3}Mn_{0.95}Co_{0.05}O_2$. Mn is blue and oxygen ions (red) are shown with anisotropic displacement ellipsoids (70%), emphasising a larger displacement along the elongated bonds.

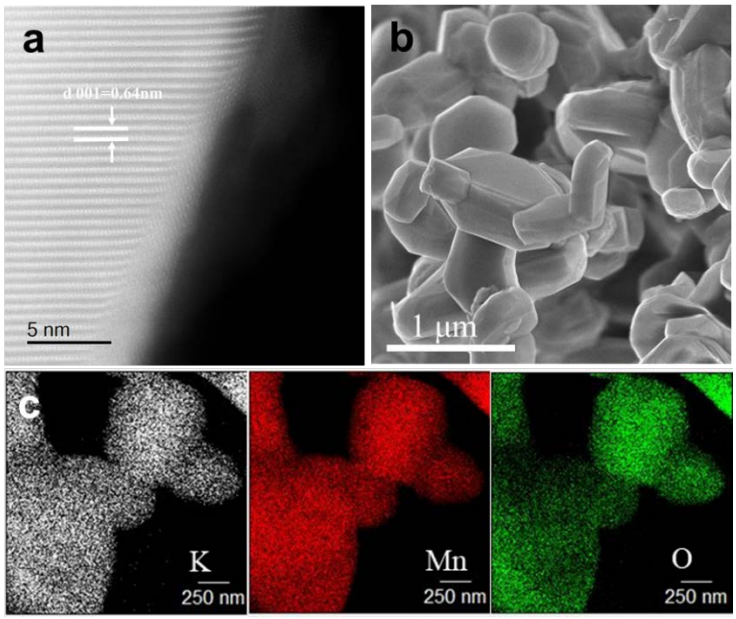

Figure S5 a) SEM image of $K_{0.3}MnO_2$ particles; b) STEM image of $K_{0.3}MnO_2$ showing (001) planes; c) Elemental distribution from EDX spectroscopy mapping of $K_{0.3}MnO_2$.

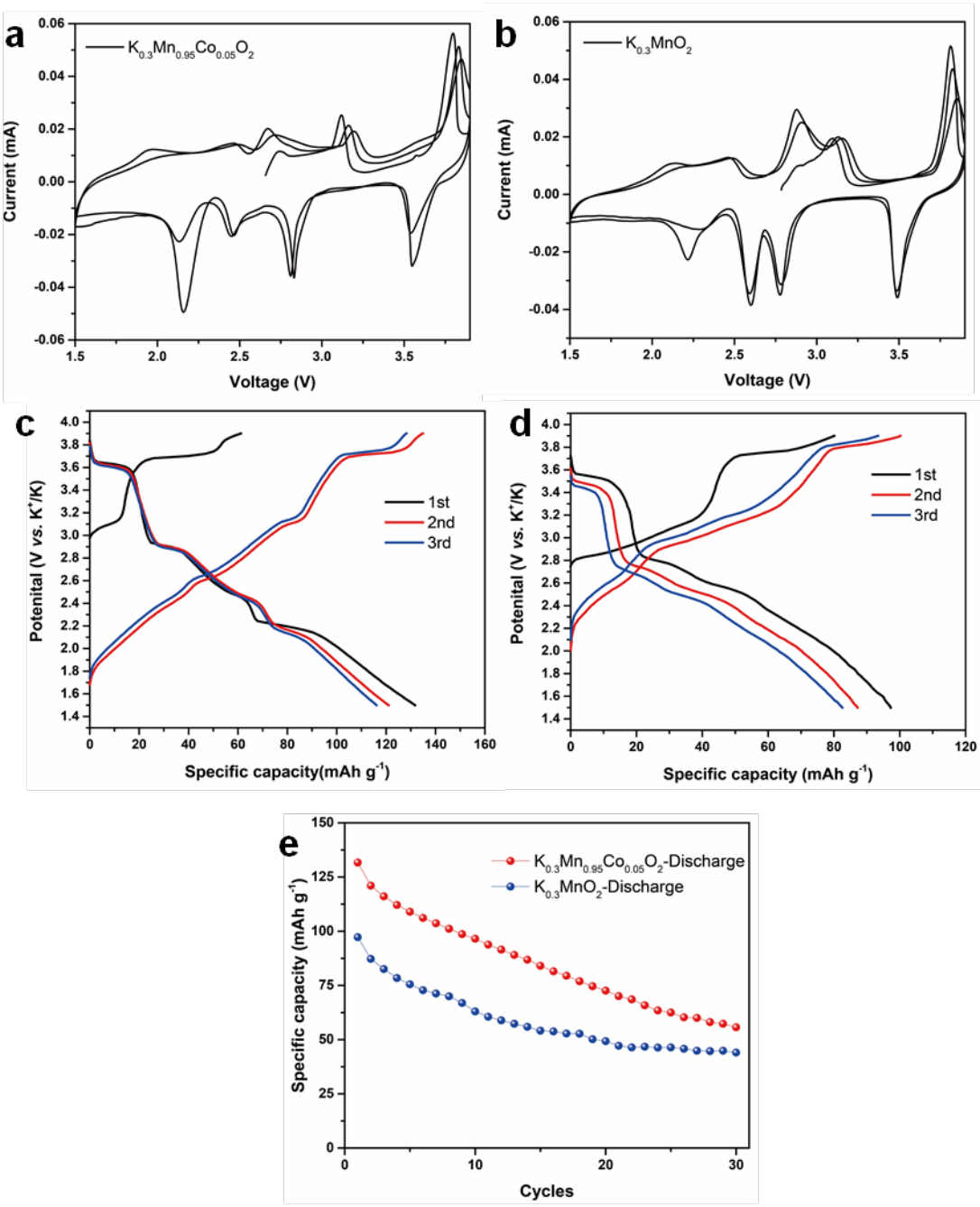

Figure S6 Cyclic voltammetry curves of a) $K_{0.3}Mn_{0.95}Co_{0.05}O_2$ and b) $K_{0.3}MnO_2$ *vs.* K in half-cells at 0.1 $mV.s^{-1}$ and galvanostatic charge/discharge profiles of c) $K_{0.3}Mn_{0.95}Co_{0.05}O_2$ and d) $K_{0.3}MnO_2$, e) discharge capacity over the first 30 cycles for $K_{0.3}Mn_{0.95}Co_{0.05}O_2$ and $K_{0.3}MnO_2$ at 22 mA g^{-1} over the extended voltage window 1.5-3.9 V.

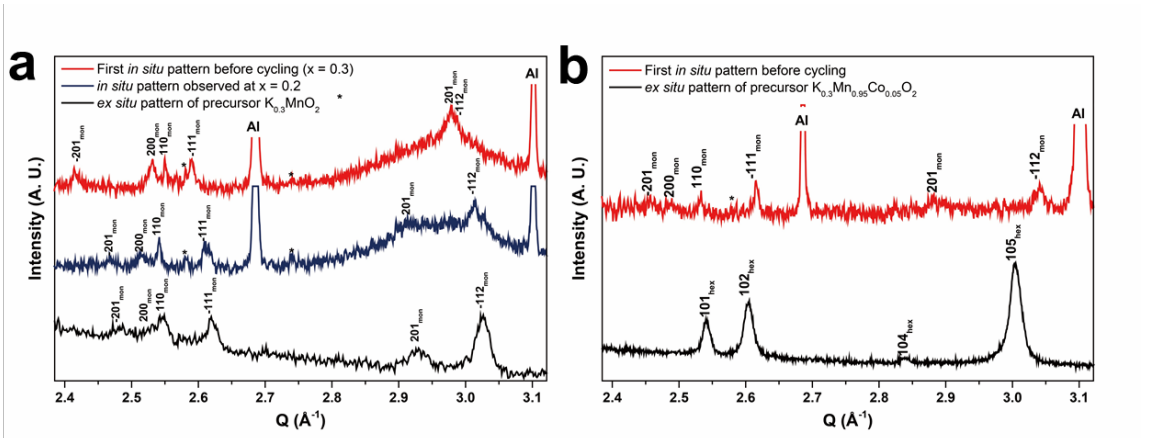

Figure S7 XRPD data of a) $K_{0.3}MnO_2$ and b) $K_{0.3}Mn_{0.95}Co_{0.05}MnO_2$ precursor powders measured *ex situ* and of the corresponding electrodes measured using *in operando* SXRPD before cycling. Reflections arising from Al metal are identified and those arising from the K_2CO_3 impurity phase are marked with an asterisk.

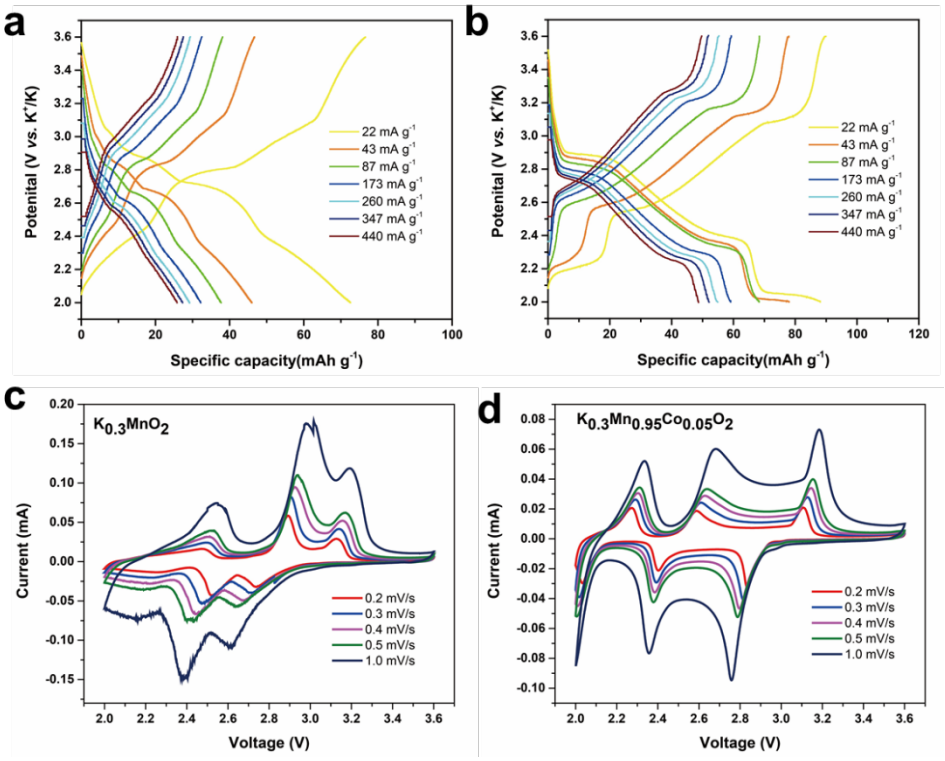

Figure S8 Galvanostatic charge/discharge curves of coin cells containing a) K_xMnO_2 and b) $K_xMn_{0.95}Co_{0.05}O_2$ under various currents measured for the 10th cycle, CV profiles of c) K_xMnO_2 and d) $K_xMn_{0.95}Co_{0.05}O_2$ at various scan rates

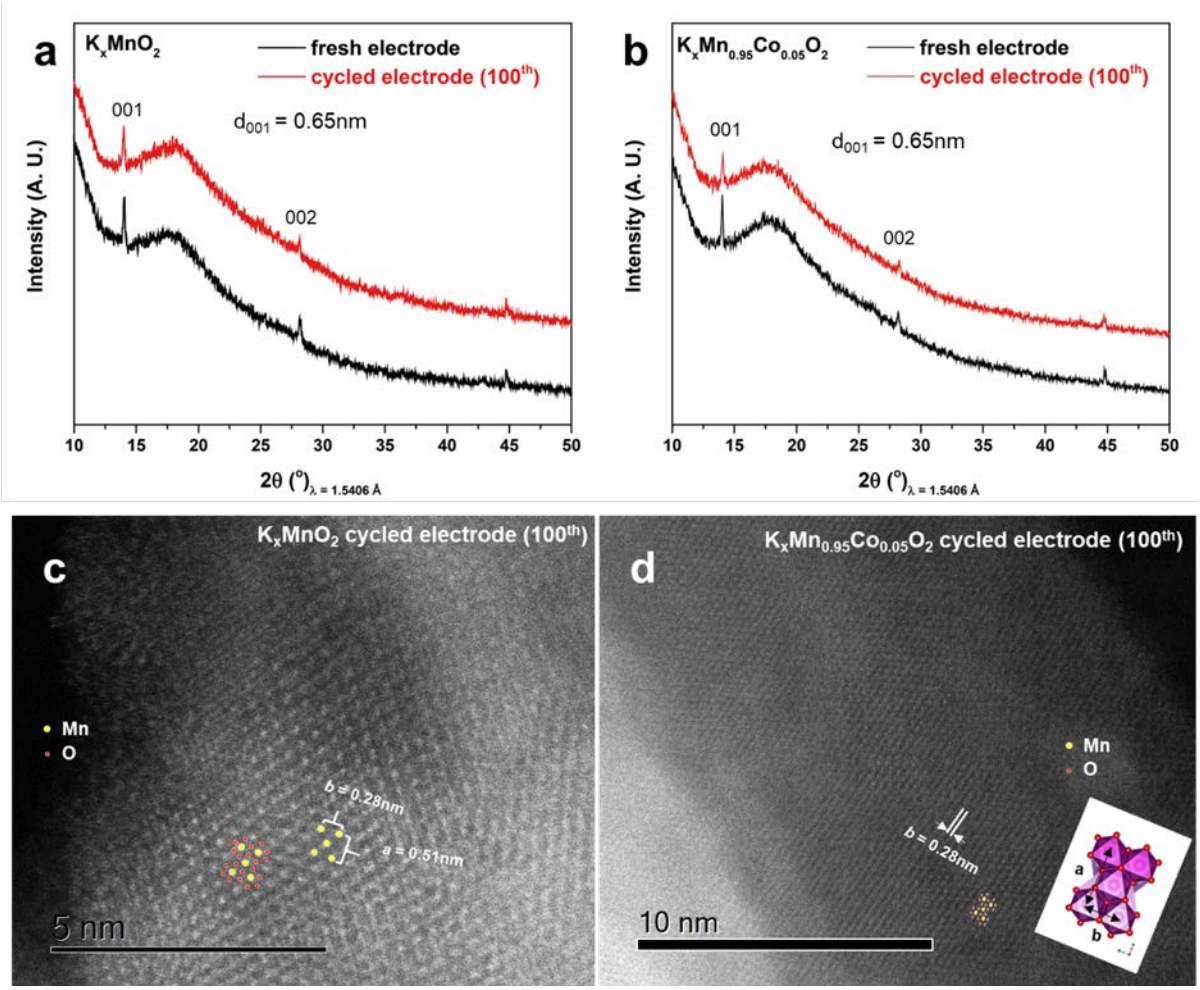

Figure S9 XRPD data of a) K_xMnO_2 and b) $K_xMn_{0.95}Co_{0.05}O_2$ before and after 100- cycles in coin cells. High-angle annular dark-field STEM images of c) K_xMnO_2 and d) $K_xMn_{0.95}Co_{0.05}O_2$ extracted from coin cells cycled 100 times.

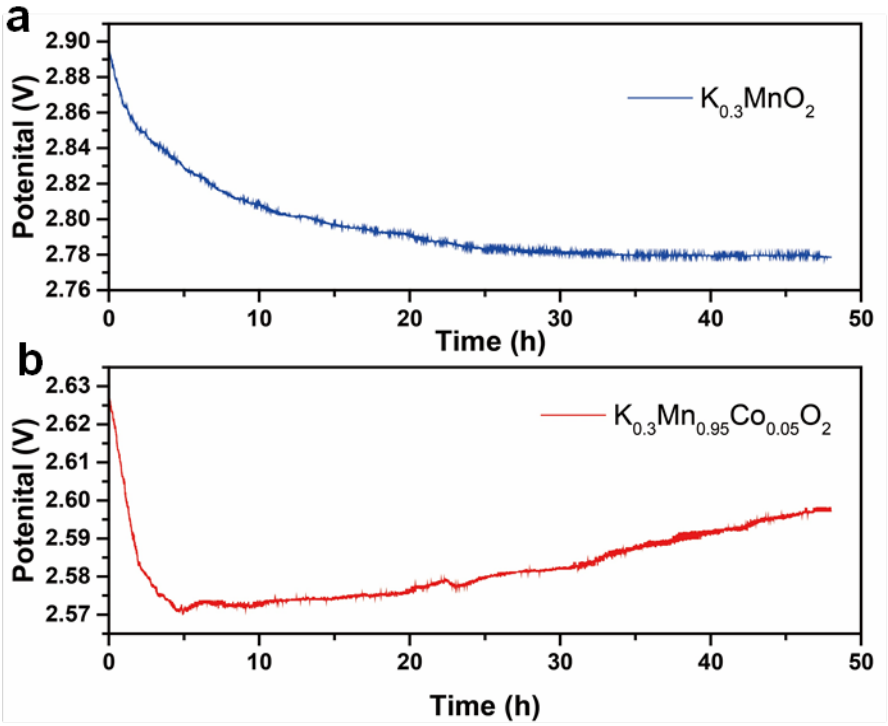

Figure S10 Open-circuit voltage *vs.* time of batteries containing a) $K_{0.3}MnO_2$ and b) $K_{0.3}Mn_{0.95}Co_{0.05}MnO_2$.

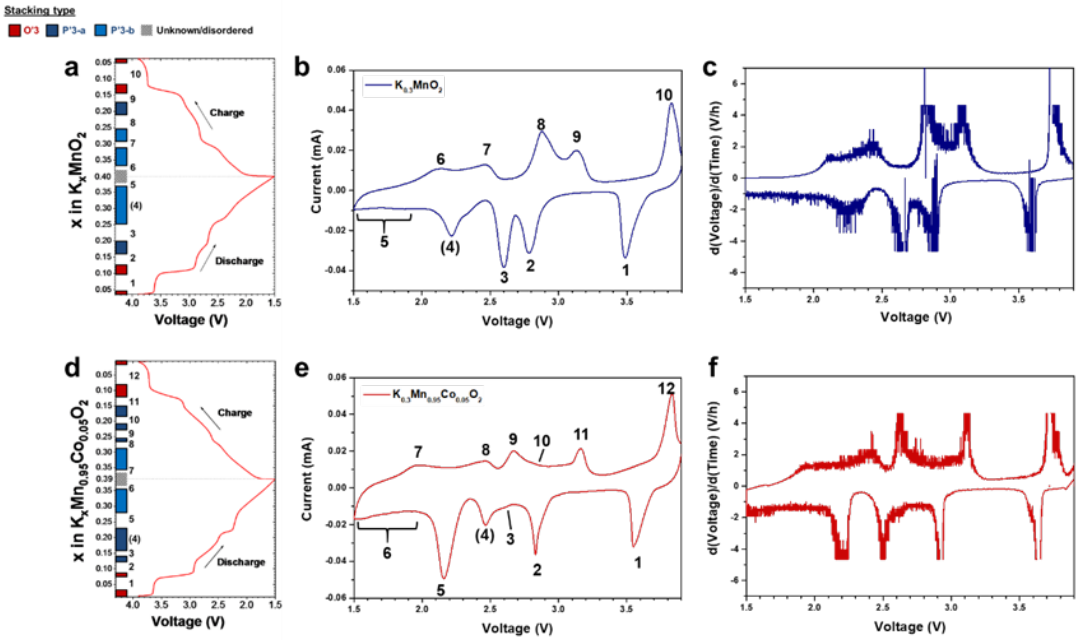

Figure S11 a) Single-phase domains determined from *in operando* synchrotron X-ray powder diffraction and the corresponding galvanostatic curve of K_xMnO_2, with numbered phase transitions between each domain. b) Cyclic voltammetry measured for K_xMnO_2 at 0.1 mV s^{-1}. c) dV/dt of K_xMnO_2. d) Single-phase domains determined from *in operando* synchrotron X-ray powder diffraction and the corresponding galvanostatic curve of $K_xMn_{0.95}Co_{0.05}O_2$, with numbered phase transitions between each domain. e) Cyclic voltammetry measured for $K_xMn_{0.95}Co_{0.05}O_2$ at 0.1 mV s^{-1}. f) dV/dt of $K_xMn_{0.95}Co_{0.05}O_2$. Transitions in parentheses signify that although a clear redox peak is visible, no obvious transition can be seen from XRPD.

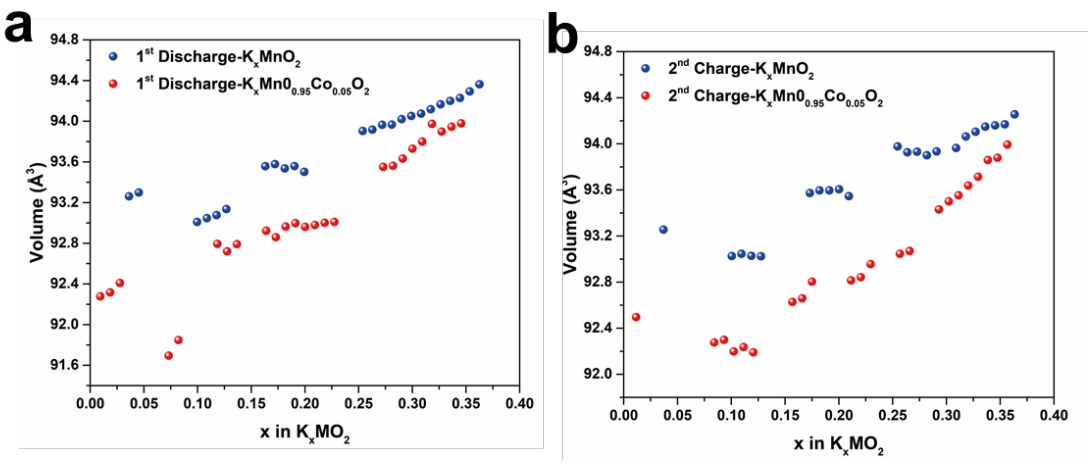

Figure S12 Volume change of K_xMnO_2 and $K_xMn_{0.95}Co_{0.05}O_2$ relative to the volume of the initial material during the a) first discharge and b) second charge.

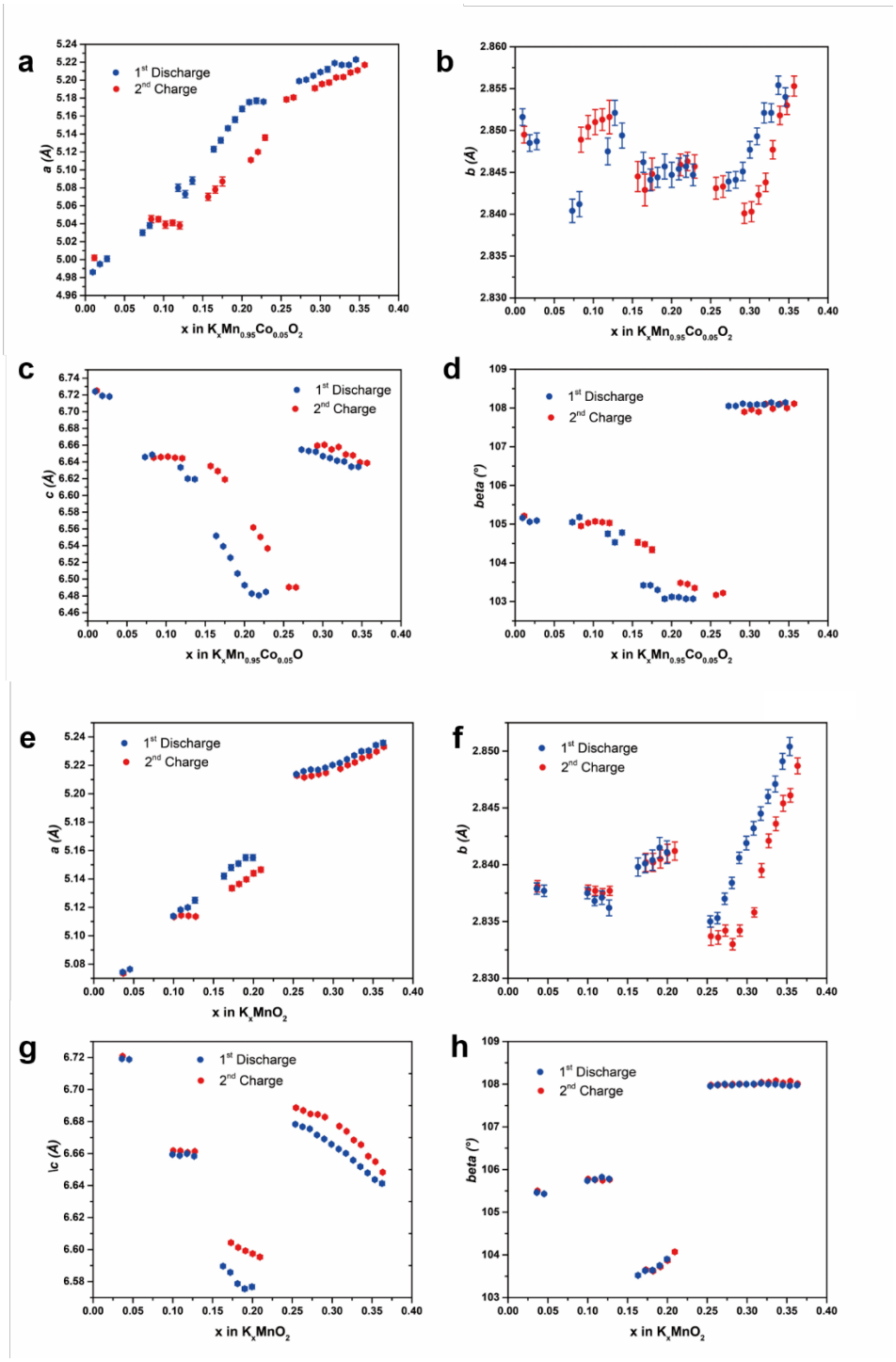

Figure S13 a) *a*, b) *b*, c) *c* and d) *β* unit-cell parameters of $K_xMn_{0.95}Co_{0.05}O_2$ and e) *a*, f) *b*, g) *c* and h) *β* of K_xMnO_2 obtained using Le Bail analysis of *in operando* SXRPD data.

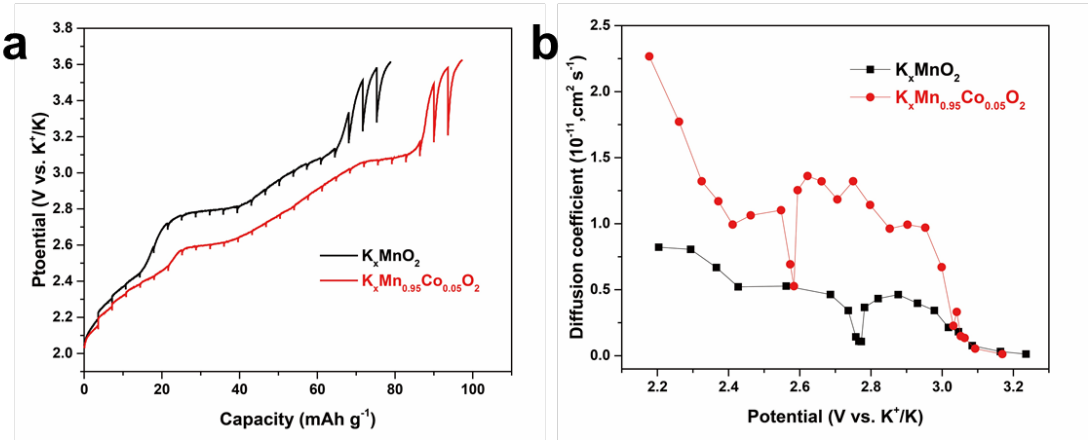

Figure S14 a) Potential profiles obtained using the GITT for K_xMnO_2 and $K_xMn_{0.95}Co_{0.05}O_2$ in coin cells during charge (depotassiation) and b) the corresponding calculated diffusion coefficient as a function of equilibrium potential.

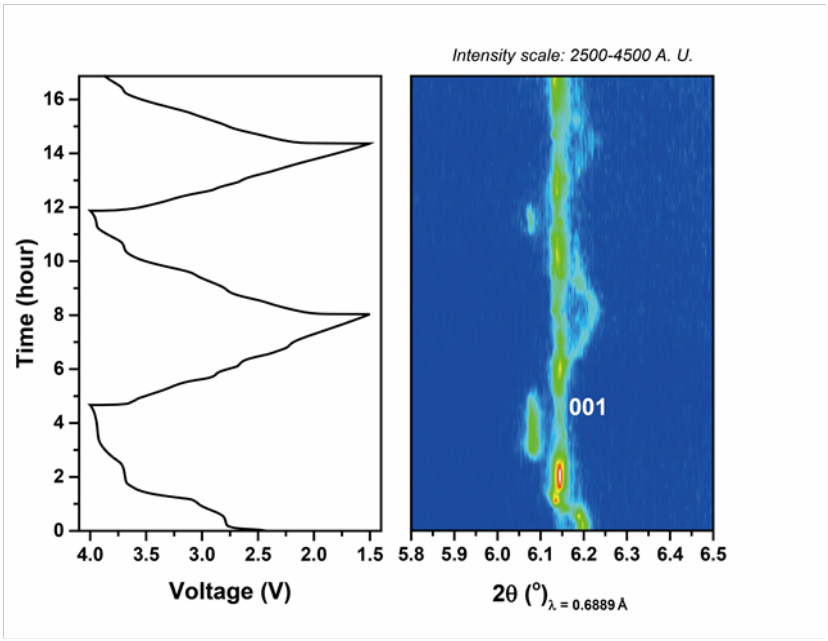

Figure S15 a) Voltage measured during the galvanostatic charge/discharge of $K_{0.3}MnO_2$ at 22 mA g^{-1} within the range 1.5-4.0 V; b) Corresponding *in operando* synchrotron X-ray powder diffraction data of the K_xMnO_2 001 reflection.

***C*2/m** *a* = 5.1313(4) Å *b* = 2.84822(13) Å *c* = 6.5976(4) Å *β* = 103.898(6)°									
Atom	**x**	**y**	**z**	**SOF***	**B_{iso} (Å^2)**	**β_{11}**	**β_{22}**	**β_{33}**	**β_{13}**
Mn	0	0	0	1	0.65(4)				
O	0.3935(4)	0	0.1571(2)	1	1.61(4)	0.0342(8)	0.0166(15)	0.0106(4)	0.0178(5)
K	0.146(4)	0	0.498(2)	0.15	3.3(3)				

Table S1 Refined atomic coordinates of the structure of $K_{0.3}MnO_2$ from joint Rietveld refinement against NPD and XRPD data with overall weighted profile R-factor R_{wp} = 2.88% and goodness-of-fit χ^2 = 2.86. Displacement parameters were refined anisotropically for the oxygen atom and the calculated equivalent isotropic parameter (B_{iso}) is given for reference. Estimated standard deviations are reported in parentheses as corrected for local correlations after Bérar and Lelann.[11] *Site occupancy factor.

$R\bar{3}m$ a = 2.88166(7) Å c = 19.1927(6) Å					
Atom	**X**	**y**	**z**	**SOF***	**B_{iso} (Å^2)**
Mn	0	0	0	0.95	0.42(4)
Co	0	0	0	=1-SOF (Mn)	= B_{iso}(Mn)
O	1/3	2/3	0.05196(5)	1	1.33(4)
K	0	0	0.1663(3)	0.15	0.98(14)

Table S2 Refined atomic coordinates of the structure of $K_{0.3}Mn_{0.95}Co_{0.05}O_2$ joint Rietveld refinement against NPD and XRPD data with overall weighted profile R-factor R_{wp} = 1.84% and goodness-of-fit χ^2 = 1.85. Estimated standard deviations are reported in parentheses as corrected for local correlations after Bérar and Lelann.[11] *Site occupancy factor.

Ion or ionic mixture M	**M-O distances for M in octahedral coordination (Å)**	**Reference**
Mn^{3+} (High-spin)	4 × 1.930 and 2 × 2.282	[11]
Mn^{4+}	1.91	[12]
Co^{3+} (Low-spin)	1.925 (averaged)	[13]
0.7 Mn^{4+} + 0.3 Mn^{3+} in $K_{0.3}MnO_2$	4 × 1.916 and 2 × 2 022	Calculated using given values
0.7 Mn^{4+} + 0.25 Mn^{3+} + 0.05 Co^{3+} in $K_{0.3}Mn_{0.95}Co_{0.05}O_2$	1.945 (averaged)	Calculated using given values

Table S3 Mn-O and Co-O distances in the literature and average distances calculated assuming $K_{0.3}MO_2$ (M = Mn + Co) composition. Despite Co^{3+} resulting in weak Jahn-Teller effects, the average value was considered as they are negligible compared to this effect for Mn^{4+}.

Cycle	Composition range (x)	Phase structure	*a* (Å)	*b* (Å)	*c* (Å)	*β* (º)
Discharge	0.03 0.04	O'3	5.074(11) 5.0764(11)	2.8379(5) 2.8377(5)	6.7192(6) 6.7188(6)	105.46(2) 105.43(2)
	0.04 0.10	2 phases				
	0.10 0.13	O'3	5.1138(11) 5.125(2)	2.8375(5) 2.8362(7)	6.6594(5) 6.6583(8)	105.740(14) 105.78(2)
	0.13 0.16	2 phases				
	0.16 0.20	P'3	5.142(2) 5.155(2)	2.8398(8) 2.841(1)	6.5896(10) 6.5767(13)	103.52(4) 103.90(4)
	0.20 0.25	2 phases				
	0.25 0.36	P'3	5.2137(8) 5.2358(16)	2.8350(5) 2.853(1)	6.6783(6) 6.6413(12)	107.958(14) 107.98(3)
	0.36 0.40	N/A (broad reflections)				
	0.36 0.31	P'3	5.2331(12) 5.2176(7)	2.8487(7) 2.8358(4)	6.6483(9) 6.6771(5)	108.01(2) 107.996(11)
	0.31 0.29	2 phases				
	0.29 0.25	P'3	5.2147(8) 5.2128(12)	2.8342(5) 2.8337(8)	6.6828(6) 6.6886(9)	108.004(14) 107.98(2)
	0.25 0.21	2 phases				
	0.21 0.17	P'3	5.147(2) 5.134(2)	2.8412(8) 2.8402(8)	6.5953(11) 6.6043(10)	104.07(4) 103.65(3)
	0.17 0.13	2 phases				
	0.13 0.10	O'3	5.1135(9) 5.1133(9)	2.8377(4) 2.8378(4)	6.6613(4) 6.6618(4)	105.765(12) 105.776(13)
	0.10 0.04	2 phases				
	0.04	O'3	5.0735(12)	2.8381(5)	6.7208(6)	105.50(2)

Table S4 Refined unit-cell parameters of K_xMnO_2 determined from Le Bail profile matching of *in operando* SXRPD data during cycling of a battery between 3.9 and 1.5 V. Compositions are rounded up to the second decimal place and estimated standard deviations are reported in parentheses as corrected for local correlations after Bérar and Lelann.[11]

Cycle	Composition range (x)	Phase structure	*a* (Å)	*b* (Å)	*c* (Å)	*β* (º)
Discharge	0.01 0.03	O'3	4.986(2) 5.001(3)	2.8516(10) 2.8487(10)	6.7241(11) 6.7181(12)	105.16(3) 105.09(3)
	0.03 0.07	2 phases				
	0.07 0.08	O'3	5.030(3) 5.038(3)	2.8404(14) 2.8412(15)	6.6458(15) 6.6485(15)	105.05(5) 105.18(5)
	0.08 0.12	2 phases				
	0.12 0.14	P'3	5.080(4) 5.088(4)	2.8475(16) 2.8494(15)	6.633(2) 6.619(2)	104.75(6) 104.78(6)
	0.14 0.16	2 phases				
	0.16 0.23	P'3	5.123(3) 5.176(2)	2.8462(12) 2.8447(13)	6.5516(14) 6.4847(13)	103.42(5) 103.07(4)
	0.23 0.27	2 phases				
	0.27 0.35	P'3	5.199(2) 5.223(2)	2.8439(11) 2.8540(11)	6.6546(15) 6.6342(15)	108.05(4) 108.14(4)
	0.35 0.39	N/A (broad reflections)				
Charge	0.39 0.36	N/A (broad reflections)				
	0.36 0.29	P'3	5.217(2) 5.191(2)	2.8553(12) 2.8401(12)	6.6387(15) 6.6594(16)	108.11(4) 107.90(4)
	0.29 0.27	2 phases				
	0.27 0.25	P'3	5.181(2) 5.179(3)	2.8433(13) 2.8431(13)	6.4902(14) 6.4904(15)	103.22(4) 103.17(4)
	0.25 0.23	2 phases				
	0.23 0.21	P'3	5.136(3) 5.111(2)	2.8457(14) 2.8459(13)	6.5367(14) 6.5617(13)	103.35(5) 103.48(4)
	0.21 0.18	2 phases				
	0.18 0.15	O'3	5.087(5) 5.070(4)	2.8448(19) 2.8445(18)	6.619(2) 6.635(2)	104.34(7) 104.53(7)
	0.15 0.12	2 phases				
	0.12 0.08	O'3	5.038(4) 5.045(4)	2.852(2) 2.8489(15)	6.644(2) 6.6451(16)	105.03(6) 104.95(5)
	0.08 0.01	2 phases				
	0.01	O'3	5.002(3)	2.8495(10)	6.7250(13)	105.21(4)

Table S5 Refined unit-cell parameters of $K_{0.3}Mn_{0.95}Co_{0.05}O_2$ determined from Le Bail profile matching of *in operando* SXRPD data during cycling of a battery between 3.9 and 1.5 V. Compositions are rounded up to the second decimal place and estimated standard deviations are reported in parentheses as corrected for local correlations after Bérar and Lelann.[11]

REFERENCES

[1] J. Kimpton, Q. Gu, *Synch. Rad. News* **2014**, 27, 18-20.

[2] Q. Gu, J. Kimpton, H. E. A. Brand, Z. Y. Wang, S. L. Chou, *Adv. Energy Mater.* **2017**, 7, 1602831.

[3] K. D. Liss, B. Hunter, M. Hagen, T. Noakes, S. Kennedy, *Physica B* **2006**, 385-386, 1010-1012.

[4] A. Belsky, M. Hellenbrandt, V. L. Karen, P. Luksch, *Acta Cryst.* **2002**, B58, 364-369.

[5] PDF-4+ 2019; ICDD: Newtown Square, PA, **2018**.

[6] V. Petříček, M. Dušek, L. *Z.* Palatinus, *Kristallogr.* **2014**, 229, 345-352.

[7] B. M. Gatehouse, D. J. Lloyd, *J. Chem. Soc., Dalton Trans.* **1973**, 70-72.

[8] C. Delmas, C. Fouassier, *Z. anorg. ally. Chem.* **1976**, 420, 184-192.

[9] E. Deiss, *Electrochim. Acta* **2005**, 50, 2927-2932.

[10] S. Zhang, Y. Zheng, X. Huang, J. Hong, B. Cao, J. Hao, Q. Fang, T. Zhou, Z. Guo, *Adv. Energy Mater.* **2019**,1900081.

[11] J. F. Bérar, P. Lelann, *J. Appl. Cryst.* **1991**, 24, 1-5.

[12] D. Jarosch, *Miner. Petrol.* **1987**, 37, 15-23.

[13] R. D. Shannon, *Acta Cryst.* **1976**, 32, 751-767.